Title	Simulation of two-way fluid-structure interaction using immersed boundary and finite element methods
Author(s)	Tuan, Mohammad Tuan Ya
Citation	大阪大学, 2009, 博士論文
Version Type	VoR
URL	https://hdl.handle.net/11094/2371
rights	
Note	

Simulation of two-way fluid-structure interaction using immersed boundary and finite element methods

TUAN YA TUAN MOHAMMAD

Department of Mechanical Engineering
OSAKA UNIVERSITY

September 2009

Abstract

A new two-way method for solving fluid-structure interaction problems is proposed by coupling immersed boundary method (IBM) and finite element method (FEM). This new method enables efficient simulation of fluid-structure interaction. Pressure and viscous forces are used for fluid and elastic body coupling. Pressure field is solved using fractional step method (FSM). An efficient pressure retrieval method is developed to allocate pressure information from the nearest fluid cell to Lagrangian points on the object's surface. At the cells occupied by a solid region, velocity field is subjected to momentum exchange procedures. The second correction of pressure is undertaken in the occupied region. The simplified marker and cell (SMAC) method is used to find scalar values for velocity and pressure correction. The present method is applied to 2-D flow fields with an elastic body to show the applicability of the method. A NACA 0012 airfoil is used as the neutral shape of the elastic object within the flow. The airfoils are initially placed in a fluid at rest with attack angle of -5°and -10°. Then, a uniform flow is given at the inlet. The coupling of IBM and FEM to study fluid and elastic body interaction problems have shown promising results. The method also shows good performance in obtaining a solution in a feasible computation time.

Acknowledgements

Contents

Chapter 1

Introduction

Various engineering problems involving fluid-structure interaction (FSI) simulations have been attracting researchers and engineers due to its significant physical relevance. However, fluid-structure interaction problems involving fluid flow and moving or deformable objects by itself is a very challenging subject. Typically, each of the fluid and solid simulations were solved independently of each other, due to complexity of the interface and limited resources in computing hardware. Even when problems were studied experimentally, thorough understanding of fluid-structure interaction has long been limited by the intricacy existing in these kinds of problems. Such problems exist in broad scope of application, ranging from chemistry (eg. particulate flow [1]), biology (motion of animals such as insect and fishes[2], heart valves and blood flow[3]), solid mechanics (flexible filament in soap film [4]) and aeroelasticity (aerodynamic loading on wings, flutter etc).

Decades of scientific research has proven that experiments are indispensable as a source of reliable data for the understanding of certain phenomena. However, setting up highly accurate and repeatable experiments requires significant investments of time and financial resources. Despite the improvements in experimentation, failures in repeatability and acquiring deeper understanding are leading the researchers to explore numerical simulations. Increasing speed and capability of current supercomputers and efficient computing techniques have promoted numerical simulation methods as an alternative to study complex and intricate physical problems. Fluid-solid interaction problems that were once out of reach for numerical studies are now feasible.

Commonly [5, 6, 7, 8, 9, 10, 11, 12, 13, 14], simulations of fluid-structure interactions involving deformable bodies were carried out using body-fitted methods based

on arbitrary Lagrangian-Eulerian (ALE) [15] to solve fluid flow and finite element method (FEM) to solve structural deformation. One example of this is simulating Parachute fluid-structure interaction [10, 11], where a very complex flow is modeled with a highly deformable object. Re-meshing of fluid domain is done whenever large deformation occurs.

Approaches in the ALE-FEM method can be divided into monolithic (fully-coupled) [5, 6, 7, 8, 9] methods and partitioned (iterative)[10, 11, 12, 13, 14] methods. With the monolithic methods, the fluid and the structural discrete equations are tightly coupled and solved together. In the partitioned methods, each field is solved separately and solution variables are passed iteratively from one field to the other until convergence is achieved. Common drawbacks of ALE-FEM may be in speed and efficiency. For objects with complex geometry, the mesh generation would not be a simple affair, and the need to re-mesh the entire computational domain each time the object deforms increases the computation load significantly.

One of the means to overcome the ALE drawback is to employ the fixed Cartesian grid for the fluid. To handle interaction between fluid and solid boundaries, the immersed boundary method (IBM) [16, 17, 18, 1, 19, 20] can be used to solve the interaction force at the occupied fluid cells by the solid. Combining Cartesian grid and IBM with FEM to solve flow field around deformable object and avoiding re-meshing of fluid domain, will produce an efficient and fast method to solve FSI. As the IBM-FEM application is being actively developed, a suitable IBM method is needed for fluid-deformable object interaction. IBM has a few different and independently methods to solve the interaction force between fluid and solid such as feed-back force [3] and body-force [17]. Peskin's [3] force generator uses rectilinear Eulerian grid for the fluid phase together with a Lagrangian representation for the immersed boundary at the object surface. The fluid and solid phases share the physical properties at the immersed boundary by mutual interpolation between Eulerian and Lagrangian references via a pseudo delta function as weight function. However, this method has two adjustable parameters for the spring-dashpot feedback force, which are unable to be determined uniquely.

In Kajishima's [17] body force method, the force between the solid and fluid is modeled by a volume fraction function of the solid volumetric fraction and the relative velocities of the two phases. This method ensures no momentum leakage between the phases as both fluid and solid share the rectilinear Eulerian grid, therefore, making interpolation unnecessary. However, continuity is affected due to changes in the

velocity field, enforced by volume averaging of the local fluid velocity and local solid velocity. Using Kajishima's method, the fluid-solid interaction is coupled by the body force. To use pressure as means of coupling of fluid-solid interaction, additional correction of pressure and velocity is needed. E. Boujo [21, 22] have explored the effect of deforming bodies on fluid using body force method. However, due to the unrobustness of the numerical procedure, the method could not deal with strong interaction between fluid and solid.

In the present study, we propose a new two-way FSI approach using IBM-FEM to solve the interaction of incompressible viscous fluid and an elastic body. Kajishima's [17] method is used to define the boundary of the structure and derive the velocity field near the elastic body. The pressure field is solved using fractional step method [23]. An efficient pressure retrieval method is also developed for the fluid-structure coupling, which would significantly reduce the number of cells needed to be scanned. Second-stage velocity and pressure corrections are proposed to take into account the effect of momentum exchange on the pressure field. Pressure and viscous force are used as surface forces on the elastic body and the deformation solved by FEM.

Chapter 2 describes the governing equation and numerical methods used in fluid-solid interaction. Validation of IBM and FEM solver are further explain in detail in Chapter 3. Chapter 4 then outlines the methods of coupling IBM-FEM while describing the computational parameters. Results of the interaction dynamics are then discussed in the latter part on Chapter 4. Finally, Chapter 5 summarizes the outcome and conclusion of this study.

Chapter 2

Basic Equation and Numerical Methods

2.1 Immersed Boundary Method

As the introduction describes, immersed boundary method (IBM) enables a fast and efficient numerical simulation of fluid-solid interaction problems. The absence of re-meshing of the computational domain by use of fixed and structured grid is possible even as the object is displaced or deformed.

In the immersed boundary method, the effect of the interface of the fluid and solid is included in the governing equations of both phases by a special interaction force term. Based on this interaction force concept, several distinctive methods have been developed depending on the definition of the interactive force, and on how Eulerian and Lagrangian variables (fluid and solid domain respectively) are connected.

IBM has a few different and independent methods to solve the interaction force between fluid and solid, such as feed-back force [3, 16], direct forcing method [18] and body-force [17]. Peskin's [3, 16] feed-back force uses rectilinear Eulerian grid for the fluid phase together with a Lagrangian representation for the immersed boundary at the object surface. The fluid and solid phases share the physical properties at the immersed boundary by mutual interpolation between Eulerian and Lagrangian references via a pseudo delta function as weight function. However, this method has two adjustable parameters for the spring-dashpot feedback force, which are unable to be determined uniquely.

Mohd-Yusoff [18] introduced a more straightforward IBM known as "direct forcing

method". In order to enforce Dirichlet conditions at the boundary, interpolations are performed between Lagrangian velocities at the solid surface and Eulerian velocities at neighboring grid points. These interpolations have proved to be quite unrobust, which is undoubtedly as obstacle for this method to become widespread for practical applications.

In Kajishima's [17] body force method, the force between the solid and fluid is modelled by a volume fraction function of the solid volumetric fraction and the relative velocities of the two phases. This method ensures no momentum leakage between the phases as both fluid and solid share the rectilinear Eulerian grid and, therefore, making interpolation unnecessary. However, continuity is affected due to changes in velocity field enforced by volume averaging of the local fluid velocity and local solid velocity. Using Kajishima's method, the fluid-solid interaction is coupled by the body force. To use pressure as means of coupling of new two-way fluid-solid interaction, additional correction of pressure and velocity is needed.

2.1.1 Basic Equation

The governing equations for incompressible fluid flow are the continuity equation and Navier-Stokes equations:

$$\nabla \cdot \boldsymbol{u}_f = 0 \tag{2.1}$$

$$\frac{\partial \boldsymbol{u}_f}{\partial t} + \boldsymbol{u}_f \cdot \nabla \boldsymbol{u}_f = -\frac{1}{\rho_f}\nabla p + \nu_f \cdot [\nabla \boldsymbol{u}_f + (\nabla \boldsymbol{u}_f)^T] \tag{2.2}$$

where u_f is fluid velocity, p is pressure, ρ_f density and ν_f is kinematic viscosity. Both density and kinematic viscosity are kept constant for this study. Equations (2.1) and (2.2) are solved by a finite difference method with the second order accuracy in space and time.

2.1.2 Fluid-Solid Interaction

For cells partially occupied by the solid structure, Kajishima et al [17] proposed an immersed boundary method that solves the momentum exchange at the fluid-structure boundary. This method is briefly described by Yuki et al [24] as follows.

A velocity field $\boldsymbol{u}$ is introduced by calculating the volume fraction and finding the local fluid velocity $\boldsymbol{u}_f$ and the local solid phase velocity $\boldsymbol{v}_p$ in each cell by:

$$\boldsymbol{u} = (1 - \alpha)\boldsymbol{u}_f + \alpha\boldsymbol{v}_p \tag{2.3}$$

where $\alpha(0 \leq \alpha \leq 1)$ is the local solid volumetric fraction in a cell as shown in Figure 2.1. The fluid-structure interaction then can be solved at the interface by assuming that the velocity field $\boldsymbol{u}$ follows the modified Navier-Stokes equations:

$$\frac{\partial\boldsymbol{u}}{\partial t} = -\frac{1}{\rho_f}\nabla p + \boldsymbol{H}_u + \boldsymbol{f}_p \tag{2.4}$$

$$\boldsymbol{H}_u = -\boldsymbol{u} \cdot \nabla\boldsymbol{u} + \nu_f\nabla \cdot [\nabla\boldsymbol{u} + (\nabla\boldsymbol{u})^T] \tag{2.5}$$

a time advancement scheme for $\boldsymbol{u}$ can be proposed as follows:

$$\boldsymbol{u}^{n+1} = \boldsymbol{u}_I - \Delta t\frac{1}{\rho_f}\nabla p + \Delta t\boldsymbol{f}_p \tag{2.6}$$

$$\boldsymbol{u}_I = \boldsymbol{u}^n + \Delta t\left(\frac{3}{2}\boldsymbol{H}_u^n - \frac{1}{2}\boldsymbol{H}_u^{n-1}\right) \tag{2.7}$$

$$\boldsymbol{f}_p = \frac{\alpha(\boldsymbol{u}_p - \boldsymbol{u}_I)}{\Delta t} \tag{2.8}$$

where superscripts n represent time step, Δt is the time increment. The body force $\boldsymbol{f}_p$ accounts for the effect of the intruder on the fluid at the interface and inside the object. It should be noted that, at $\alpha = 0$ where zero interaction force ($\boldsymbol{f}_p = 0$) is enforced, the above time advancement is then carried by second-order Adam-Bashforth method and the SMAC method for a single-phase fluid.

In the present study, the numerical schemes are modified, as pressure is used to couple the fluid-structure interaction. The body force $\boldsymbol{f}_p$ is dropped from Equation (2.4). The following equations describe velocity field $\boldsymbol{u}_f$, assuming it follows the Navier-Stokes equations:

$$\frac{\partial\boldsymbol{u}_f}{\partial t} = -\frac{1}{\rho_f}\nabla p + \boldsymbol{H}_u \tag{2.9}$$

$$\boldsymbol{H}_u = -\boldsymbol{u}_f \cdot \nabla\boldsymbol{u}_f + \nu_f\nabla \cdot [\nabla\boldsymbol{u}_f + (\nabla\boldsymbol{u}_f)^T] \tag{2.10}$$

a time advancement scheme for $\boldsymbol{u}_f$ can be proposed as follows:

$$\boldsymbol{u}_I \;=\; \boldsymbol{u}_f^n + \Delta t \left(\frac{3}{2} \boldsymbol{H}_u^n - \frac{1}{2} \boldsymbol{H}_u^{n-1} \right) \tag{2.11}$$

$$\frac{1}{\rho_f} \nabla^2 p^{n+1} \;=\; \frac{\nabla \cdot \boldsymbol{u}_I}{\Delta t} \tag{2.12}$$

$$\boldsymbol{u}_f^{n+1} \;=\; \boldsymbol{u}_I - \Delta t \frac{1}{\rho_f} \nabla p^{n+1} \tag{2.13}$$

where superscripts n represent time, Δt is the time increment and $\boldsymbol{u}_I$ is intermediate velocity. Time advancement is then carried by second-order Adam-Bashforth method and Fractional Step Method as a single continuum. A Poisson equation is then solved with the divergence of the intermediate velocity $\boldsymbol{u}_I$ as a source term to provide a pressure p^{n+1}, which is then used to correct the intermediate velocity, providing a divergence free velocity $\boldsymbol{u}_f^{n+1}$ and integration proceeding to the next time step.
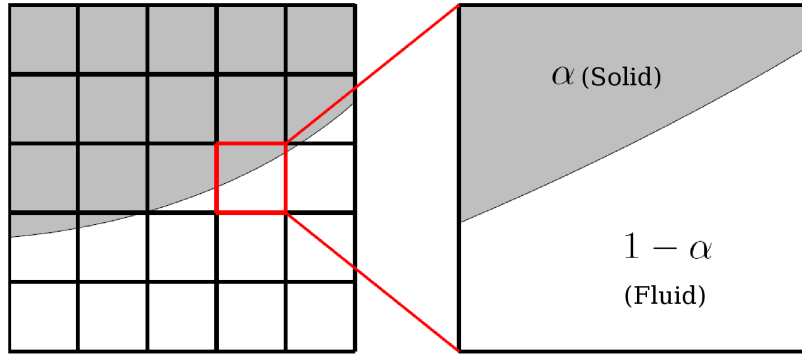
Figure 2.1: Uniform Cartesian grid for IBM and definition of solid volumetric fraction α

2.1.3   Surface Digitizer

To apply immersed boundary method, a suitable and efficient surface digitizer is required. This is due to the requirement that each solid volumetric fraction is needed to be evaluated at each cell. Originally, Kajishima et al.[17] developed and used an efficient method specifically for spherical objects. Recently, Yuki et al [24] have simplified and improved the digitizer to also enable it for use of arbitrarily shaped objects. It is based on the following hyperbolic-tangent function to digitize the fluid-

solid interface for obtaining α:

$$\alpha = \frac{1}{2}\left\{ 1 - tanh\left(\frac{\delta s}{\sigma\lambda\Delta}\right)\right\} \tag{2.14}$$

$$\lambda = |n_x| + |n_y| + |n_z| \tag{2.15}$$

$$\sigma = 0.05(1 - \lambda^2) + 0.3 \tag{2.16}$$

where $n = (n_x, n_y, n_z)$ is a normal outward unit vector at a surface element and δs is a signed distance from the cell center to the surface element and Δ is cell size uniformly distributed over the computational domain. This digitizer was proven to be accurate when the surface digitiser was used to evaluate the particle volume with 20 and 16 cells covering the diameter of spherical particle, Equation (2.14) gives 0.26% and 0.43% in error respectively. Also from the simplified formulation, the digitiser was able to reduce the processing time by 25% compared to the original digitiser.

2.2 Two-Stage Correction of Velocity and Pressure

Velocity field of the fluid cells occupied by solid region will be derived by volume averaging the local fluid velocity $\boldsymbol{u}_f$ and the local solid phase velocity $\boldsymbol{v}_p$ force described by Equation (2.3). Careful treatment is needed for derivation of pressure field affected by this change as it will affect the two-way fluid-solid interaction. As pressure field is not corrected during velocity field volume averaging, a second derivative of pressure is undertaken at the cells that are affected. Figure 2.2 shows the complete procedure of two-stage correction of velocity and pressure. A small domain as Figure 2.3, bounding the near region of the object is chosen for the correction.

Velocity field $\boldsymbol{u}_1^n$ at the current time step n, is first introduce to derive for the next time step $n + 1$. The intermediate velocity, $\boldsymbol{u}_I$ is first derived by the second-order Adam-Bashforth method (Equation (2.17)). A Poisson equation (Equation (2.18)) is then solved with the divergence of the intermediate velocity $\boldsymbol{u}_I$ as a source term to provide a pressure p_1^{n+1}:

$$\boldsymbol{u}_I = \boldsymbol{u}_1^n + \Delta t\left(\frac{3}{2}\boldsymbol{H}_{u_1}^n - \frac{1}{2}\boldsymbol{H}_{u_1}^{n-1}\right) \tag{2.17}$$

$$\frac{1}{\rho_f}\nabla^2 p_1^{n+1} = \frac{\nabla \cdot \boldsymbol{u}_I}{\Delta t} \tag{2.18}$$

which is then used to correct the intermediate velocity of Equation (2.17), providing a divergence free velocity $\boldsymbol{u}_1^{n+1}$.

$$\boldsymbol{u}_1^{n+1} = \boldsymbol{u}_I - \Delta t \frac{1}{\rho_f} \nabla p^{n+1} \tag{2.19}$$

A velocity field $\boldsymbol{u}_2^{n+1}$ is derived by the volume averaging the local fluid velocity $\boldsymbol{u}_f$ and the local solid phase velocity $\boldsymbol{v}_p$ in each fluid cell that is partially or fully occupied by solid cell, as shown in Equation (2.20).

$$\boldsymbol{u}_2^{n+1} = (1 - \alpha)\boldsymbol{u}_1^{n+1} + \alpha\boldsymbol{v}_p^{n+1} \tag{2.20}$$

Since there is significant modification of the velocity field, the value of pressure should also reflect these changes. Hence the development of the second-stage correction. This procedure is also applied to fluid cells that are partially or fully occupied by solid cells bounded by a region called small domain in Figure 2.3. Firstly, in Equation (2.21), the SMAC method is used to find the scalar potential, ϕ^{n+1}. ϕ^{n+1} then used as the velocity and pressure correction factor as shown in Equation (2.22) and (2.23) to obtain $\boldsymbol{u}_3^{n+1}, p_2^{n+1}$.

$$\frac{1}{\rho_f} \nabla^2 \phi^{n+1} = \frac{\nabla \cdot \boldsymbol{u}_2^{n+1}}{\Delta t} \tag{2.21}$$

$$\boldsymbol{u}_3^{n+1} = \boldsymbol{u}_2^{n+1} - \Delta t \frac{1}{\rho_f} \nabla \phi^{n+1} \tag{2.22}$$

$$p_2^{n+1} = p_1^{n+1} + \phi^{n+1} \tag{2.23}$$

where $\boldsymbol{u}_3^{n+1}$ and p_2^{n+1} are velocity and pressure that satisfies continuity equation. The velocity and pressure fields are used for the next time step.

2.3 Finite Element Method

2.3.1 Basic Equations

For solid phase, Navier's equation which governs the solid's displacement is used for a homogeneous isotropic elastic material under plane strain condition.

$$\rho \frac{\partial^2 z_i}{\partial t^2} = \frac{\partial \sigma_{ij}}{\partial x_j} + F_i \tag{2.24}$$

9

Start / Continue   ←   **FEM**

$u_1{}^n$

Fractional Step Method

$$u_I = u_1{}^n + \Delta t\,\frac{\left(3H_{u_1}^n - H_{u_1}^{n-1}\right)}{2}$$

$$\frac{1}{\rho_f}\nabla^2 p_1{}^{n+1} = \frac{\nabla \cdot u_I}{\Delta t}$$

$u_1{}^n,\ p_1{}^n$

Velocity correction

$$u_1{}^{n+1} = u_I - \Delta t\,\frac{1}{\rho_f}\nabla p_1{}^{n+1}$$

$u_1{}^{n+1},\ p_1{}^{n+1}$

Velocity field volume averaging

$$u_2{}^{n+1} = (1-\alpha)u_1{}^{n+1} + \alpha v_p$$

$u_3{}^{n+1},\ p_2{}^{n+1}$

Velocity and pressure correction

$$u_3{}^{n+1} = u_2{}^{n+1} - \Delta t\,\frac{1}{\rho_f}\nabla \phi^{n+1}$$

$$p_2{}^{n+1} = p_1{}^{n+1} + \phi^{n+1}$$

$u_2{}^{n+1},\ \phi^{n+1}$

SMAC method

$$\frac{1}{\rho_f}\nabla^2 \phi^{n+1} = \frac{\nabla \cdot u_2{}^{n+1}}{\Delta t}$$

$u_2{}^{n+1},\ p_1{}^{n+1}$

Small domain
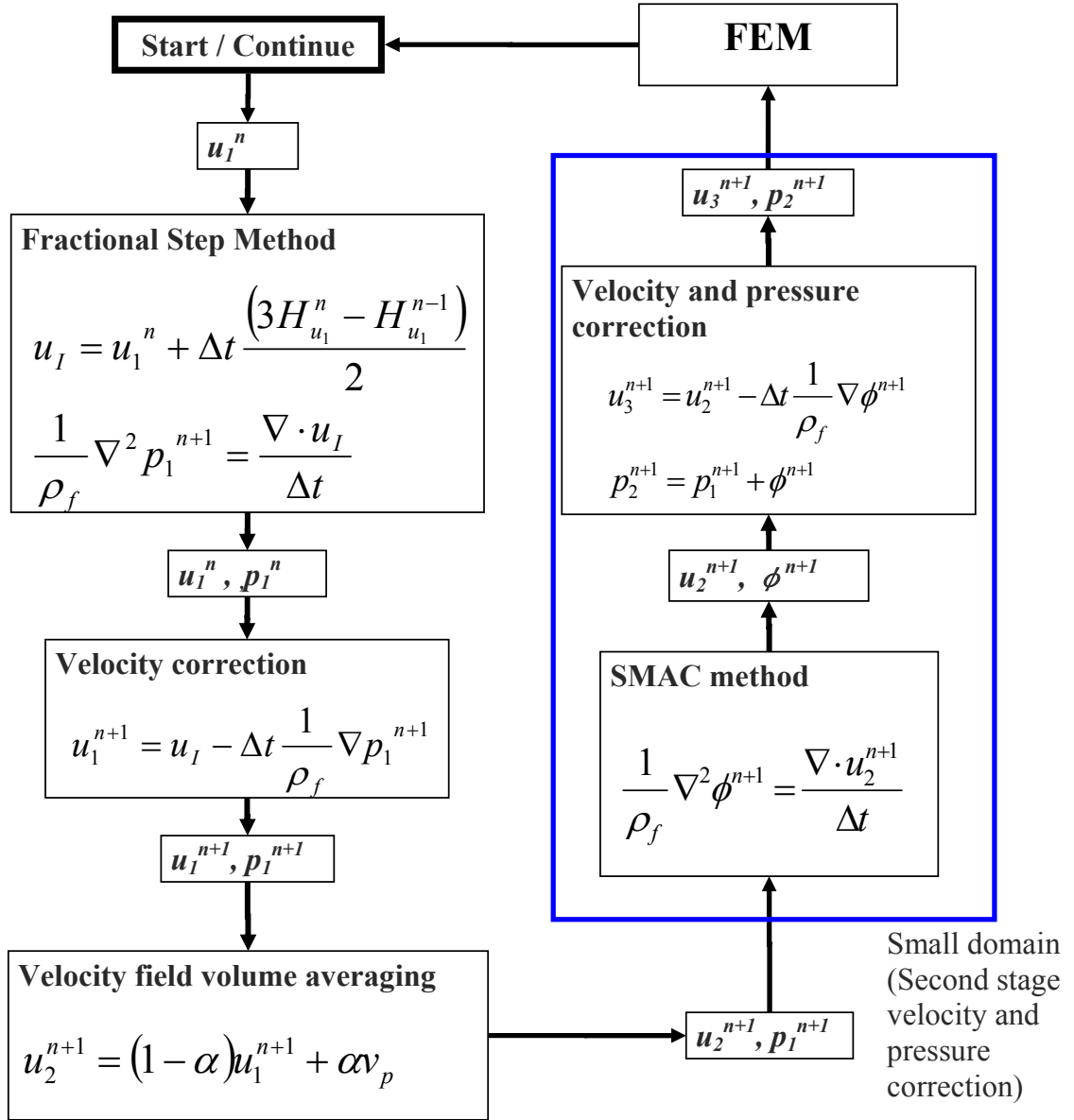(Second stage
velocity and
pressure
correction)

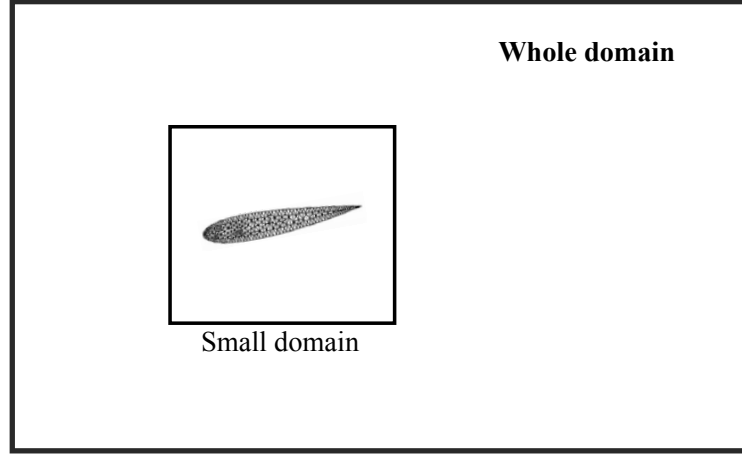Figure 2.2: Two-stage velocity and pressure correction algorithm

Figure 2.3: Schematic showing the small domain

where ρ is density, r_i displacement, t time, σ_{ij} stress tensor, x_j coordinate, and F_i external force. The equation is discretized by a weighted residual method and results in a linear matrix system which is shown as follows:

$$\mathbf{M}\ddot{\boldsymbol{z}} + \mathbf{K}\boldsymbol{z} = \mathbf{F} \tag{2.25}$$

where $\mathbf{M}$ is global mass matrix, $\mathbf{K}$ is global stiffness matrix, and $\boldsymbol{z}$ is the global displacement vector. Wilson-θ method is used for the time advancement. Generally, external forces $\mathbf{F}$ are the summation of the surface force components $\mathbf{t}$ and volume force components $\mathbf{f}$ over all boundary elements Ω_b and volume elements V_e are shown by the following equation:

$$\mathbf{F} = \sum_b \int_{\Omega_b} \mathbf{N}^T \mathbf{t} \, \mathrm{d}\Omega + \sum_e \int_{V_e} \mathbf{N}^T \mathbf{f} \, \mathrm{d}V \tag{2.26}$$

where $\mathbf{N}$ is the shape functions, and $\mathrm{d}\Omega$, the boundary elements. In the present study, only one method of application of fluid forces has been considered, by explicitly computing the fluid pressure and viscous forces and applying them as the surface forces.

$$\{\mathbf{t}\} = \begin{Bmatrix} T_x \\ T_y \end{Bmatrix} \tag{2.27}$$

11

The fluid and the deformable object are linked by the fluid pressure p in Equation (2.23) and viscous force, $(\nu_f \cdot [\nabla u_f + (\nabla u_f)^T])$ to surface forces $\{\mathbf{t}\}$ in Equation (2.27) as follows:

$$\begin{Bmatrix} T_x \\ T_y \end{Bmatrix} = \left(p + \nu_f \cdot [\nabla u_f + (\nabla u_f)^T] \right) \begin{Bmatrix} n_x \\ n_y \end{Bmatrix} \tag{2.28}$$

where $\{n_x, n_y\}^T$ is outward normal vector at boundary Ω.

2.3.2 Damping

Modeling the dynamics of the solid phase using Navier's Equation (2.24) led to the basic second-order propagation Equation (2.25). However, damping, which all actual solids in motion experience (together with elastic and inertial forces), are not included in this ideal modeling. Damping essentially dissipates energy for solids which includes internal and structural damping. Internal damping is primarily due to micro-structure imperfection, dislocation, and thermoplastic effects etc. in the material. Among internal damping there are generally distinguished viscoelastic damping, which depend on the frequency of the oscillation, and hysteresis damping which does not. Meanwhile structural damping is due to friction at the contacting surfaces of different elements. Despite damping phenomena being non-linear, it is common to linearize dissipative forces, for example, by assuming that they are proportional to velocity, leading to the following equation of motion:

$$\mathbf{M}\ddot{z} + \mathbf{C}\dot{z} + \mathbf{K}z = \mathbf{F} \tag{2.29}$$

where $\mathbf{C}$ is the damping matrix. Although $\mathbf{C}$ is generally measured or assessed for a particular mechanical system, one simple and common way to model damping is to assume that the damping matrix can be taken as a linear combination of the mass and stiffness matrices as:

$$\mathbf{C} = f_m\mathbf{M} + f_k\mathbf{K} \tag{2.30}$$

and f_m and f_k are called 'Rayleigh damping coefficients'. These coefficients can be related by using damping ratio equation shown as follows:

$$\zeta = \frac{f_m + f_k\omega^2}{2\omega} \tag{2.31}$$

where $\omega = 2\pi f_n$ and f_n is the natural frequency.

2.4 Coupling of IBM-FEM

In the Section 2.1.2, the effect of solid on fluid phase and also its implementation has been outlined in detail. However, the influence of fluid on solid needs to be explained here. In the present study, the application of fluid forces to the solid is through calculation of pressure and viscous forces. As the Lagrangian coordinates (solid mesh) do not exactly coincide with Eulerian coordinates (fluid cells), an efficient and yet sufficiently accurate method for pressure retrieval is required. However, special interpolation techniques are not developed during this study, as these techniques require further in-depth investigation.

2.4.1 Pressure and Viscous Forces

Since velocity and pressure fields are known, it is possible to compute pressure and viscous forces acting at any point of the fluid-solid interface, and to apply them as external forces $\mathbf{t}$ in Equation 2.26:

$$\mathbf{t} = -p_w n_\perp + \tau_w n_\parallel \tag{2.32}$$

where $n_\perp$ is the normal outward unit vector at the surface, $n_\parallel$ is the unit vector parallel to the surface and oriented downstream, and p_w and τ_w are respectively pressure and shear stress at the surface (the subscript w stands for "wall"). With this approach, no volume force is applied to the solid: $f_p = 0$.

2.4.2 Pressure Retrieval Method

A method is developed to retrieve pressure information from the nearest fluid cell to a Lagrangian point on the object's surface. For each node on the surface of the FEM mesh, the method scans a 3×3-mesh around the cell to which the node belongs. Figure 2.4 is the schematic of this scanning method. Let $\overrightarrow{\mathbf{A}}$ be the vector between node j and cell center, and $\mathbf{n}$ the normal vector at node j. Angle between $\overrightarrow{\mathbf{A}}$ and $\mathbf{n}$ is θ where

$$\theta = \arccos\left(\frac{\overrightarrow{\mathbf{A}} \cdot \mathbf{n}}{|\overrightarrow{\mathbf{A}}||\mathbf{n}|}\right) \tag{2.33}$$

The cell center is within the fluid domain when $\theta \leq 90°$. The pressure value at the nearest point outside the object is allocated to the Lagrangian point at the object

surface. This method ensures that pressure is assigned for an object with multiple interfaces within one unit cell. However, the cells size need to be sufficiently fine so that the pressure values assigned are reasonably accurate without the need for an interpolation scheme.
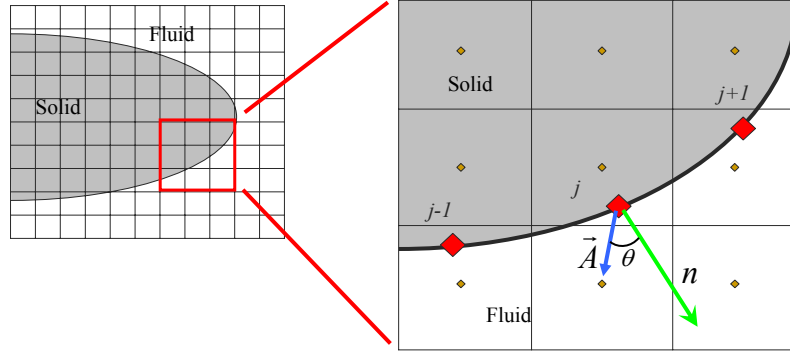

Figure 2.4: Schematic of pressure scanning method

Chapter 3

Validation

In this study, IBM and FEM were validated independently before proceeding to combine both codes. The numerical setup for IBM validation is described, followed by a discussion of C_p plots of XFOIL [25], two-stage correction method and the original Fractional Step Method. For FEM validation, the solver is used to solve for free oscillation eigenfrequencies and also the deflection of a beam under a gravitational field.

3.1 IBM Validation

3.1.1 Numerical Setup for Validation

For the validation, the computational domain length and height are $7L$ and $3L$ respectively where L is the chord length of the airfoil as show in Figure 3.1. The object is a NACA0012 symmetric airfoil. The leading edge of airfoil is located at $x = 3L$ from the inlet. Table 3.1 shows the parameters used for the validation of fluid flow using IBM. The Cartesian grid size, Δx and $\Delta y = 0.01$ with the number of cells $n_x \times n_y = 700 \times 300$. The time step is $\Delta t = 0.003s$, the free stream velocity, $U_o = 1m/s$. By estimating the boundary thickness to be approximately $5\sqrt{\frac{\nu L}{U_o}}$, the mesh size Δx and Δy is much smaller then boundary layer when the Reynolds numbers are, $Re = 500$ and 1000.
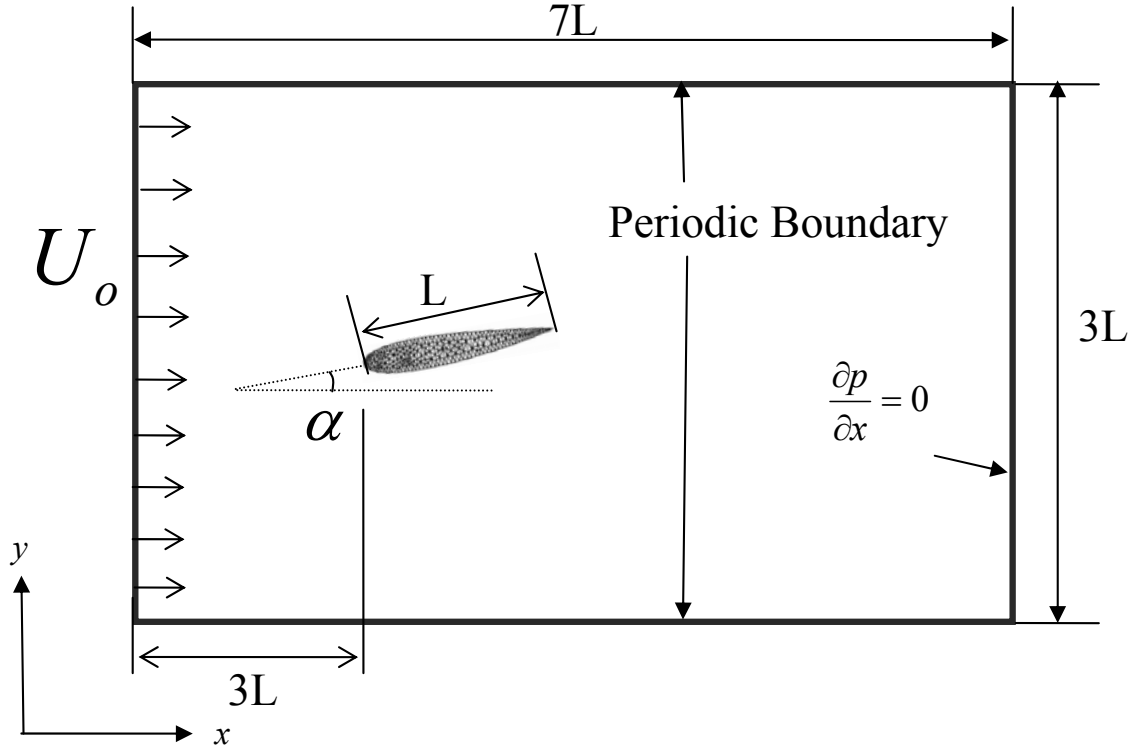
Figure 3.1: Schematics of computational domain for validation

Table 3.1: Computational setup for validation.

Fluid parameters	
Number of grid point	700×300
Reynolds number, $Re\left(\frac{U_oL}{\nu}\right)$	$500, 1000$
Time increment, Δt	0.003
Grid size,$\Delta x, \Delta y$	0.01
Angle of incidence, α	$0^o, -5^o$

3.1.2 Pressure Coefficient Plots

Pressure coefficients, C_p plots are simple means to gain an insight into the flow field of the fluid flow and validate a computational method simulating airfoil and fluid flow. It is defined as:

$$C_p = \frac{p - p_o}{\frac{1}{2}\rho_o U_o^2} = \frac{p - p_o}{q_o} \tag{3.1}$$

where p and p_o is the local and free stream pressure respectively. Local pressure p is derived from the closest fluid cell to the surface of the airfoil as the pressure retrieval method described. Figure 3.2 and 3.3 show results of pressure coefficient C_p against chord length x/c at $Re = 500$ and 1000 with angle of incidence $0°$ and $5°$. Three sets of results are presented in each figures, with two sets from IBM (Fractional Step Method with two-stage correction and Fractional Step Method without correction) and another set from XFOIL [25] software, which is based on a panel method and designed to analyze subsonic airfoils and used as the benchmark.

When the angle of incidence is $0°$, IBM with two-stage correction shows a very good agreement with XFOIL data for both $Re = 500$ and 1000. However, when $Re = 1000$, the C_p values near the leading edge show some discrepancies with XFOIL data. On the contrary, IBM without two-stage correction show very large disagreement with the XFOIL and also two-stage correction plots. The errors vary from 67% near the leading edge to 37% at the trailing edge. For $Re = 1000$, the error increases to 71% near the leading edge and 37% at the trailing edge. This discrepancies really shows the need of two-stage correction method. In the original method, the local pressure field p that affected by the Equation (2.3) are not corrected and the absent of forcing term f_p possibly lead to such error.

For a $5°$ angle of incidence plot, IBM without any correction continues the previous outcome of significant differences with XFOIL data. The plot of two-stage correction has generally good agreement with XFOIL. However, near the trailing edge, some discrepancies with XFOIL exist. This highlights the known limitation of IBM to solve flow near the thin/sharp edges, which is also known as Kutta-condition. Kutta-condition exists when air flowing over the topside and air flowing under the bottom side meet at the sharp trailing edge. There is no flow of air around the trailing edge and forward towards the leading edge. As an airfoil with sharp trailing edge begins to move with a positive angle of attack, the air passing the bottom side of the airfoil reaches trailing edge and must flow around the trailing edge and along the

17

topside of the airfoil towards the stagnation point. Inability to properly solve this condition would affect the overall results of C_p distribution. However, since the error is considerably small, IBM with two-stage correction method is very much capable for further development in this study.

3.2   FEM Validation

The solid phase solver is shared with the work of Edouard Boujo [22] which validate it through consideration of free oscillation eigenfrequecies. Simulation results for an elastic beam were compared to theoretical predictions from the oscillation theory.

The deflection of a beam in gravitational field was also simulated to validate the external volume forces such as the interaction force.

3.2.1   Free-Oscillation

In the case of free oscillation, an elastic beam of rectangular cross-section is investigated, with one of the beam's ends fixed in space (clamped condition). Theoretical eigenfrequencies f_n^* under free-oscillation (no external force) are given by [26]:

$$f_n^* = \frac{A_n \pi}{16\sqrt{3}} \frac{T}{L^2} \sqrt{\frac{E}{\rho_s}} \tag{3.2}$$

where n is the oscillation mode, T is the beam thickness, L is the beam length E and ρ_s are Young's modulus and density of the material respectively, and A_n coefficients are given as follows:

$$A_n = \begin{cases} 1.194^2, & n = 1, \\ 2.988^2, & n = 2, \\ (2n-1)^2, & n \geq 3. \end{cases} \tag{3.3}$$

The concept of free-oscillation eigenfrequencies and eigenmodes is based on the assumption that the deformation of the object can be described as a linear combination of harmonic functions of time:

$$z(x,t) = \sum_{n=1}^{\infty} z_n(x,t) = \sum_{n=1}^{\infty} \hat{z}_n(x) cos(\omega_n t + \varphi_n) \tag{3.4}$$

or in complex notation:

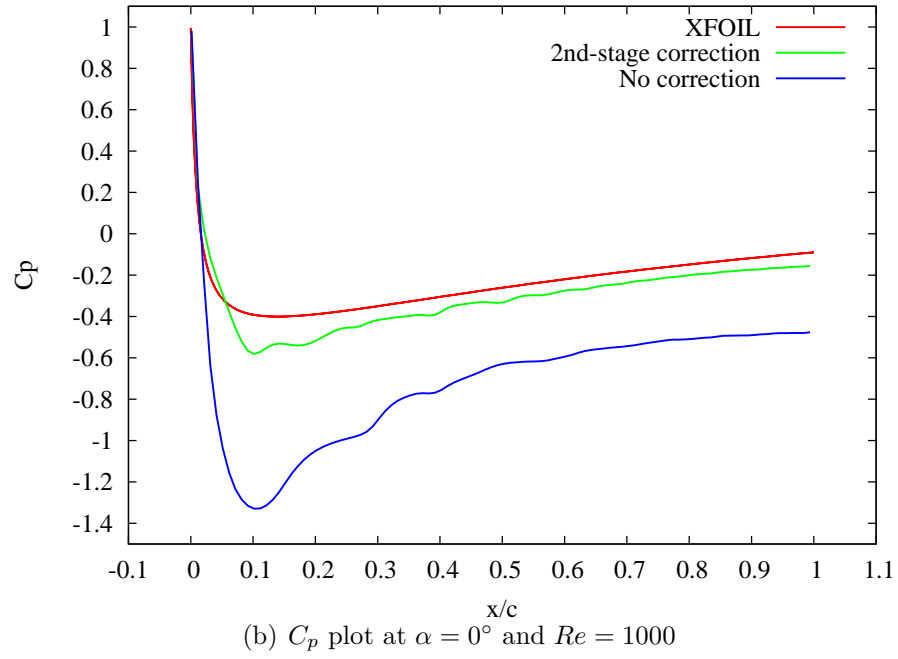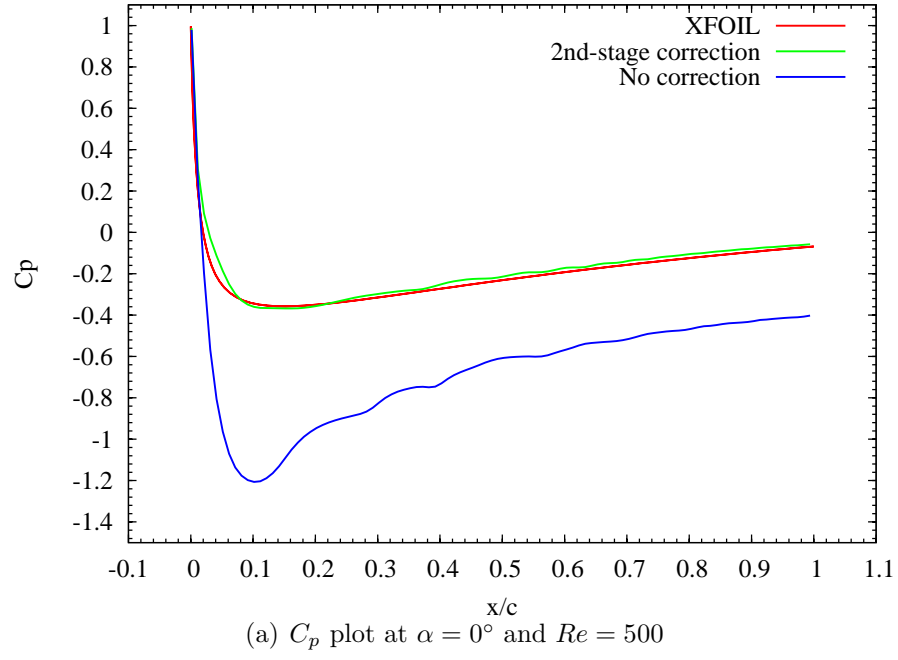(a) C_p plot at $\alpha = 0°$ and $Re = 500$

(b) C_p plot at $\alpha = 0°$ and $Re = 1000$

Figure 3.2: Plots of C_p against x/c for NACA0012 at $0°$ angle of incidence

19

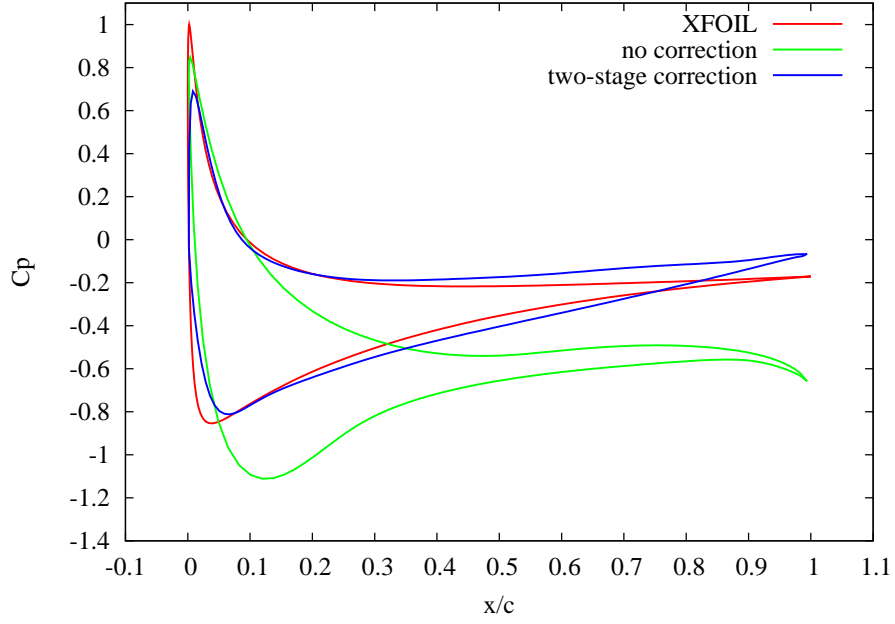Figure 3.3: Plots of C_p against x/c for NACA0012 at 5° and $Re = 500$

$$z(x,t) = \sum_{n=1}^{\infty} z_n(x,t) = \sum_{n=1}^{\infty} \hat{z}_n(x)e^{i(\omega_n t + \varphi_n)} \tag{3.5}$$

which define the whole system oscillating at the same frequency with each mode being a unique solution of equation of motion. For a certain mode n, substituting $\ddot{z}_n = -\omega_n^2 z_n$ into the undamped equation of motion (2.25) without the external force gives:

$$(K - \omega_n^2 M)\hat{z}_n = 0 \tag{3.6}$$

which is an eigenvalue problem. For each mode n, the solution of (3.6) is made of the eigenvalue ω_n^2 and the eigenvector $\hat{z}_n$ which describes the frequency $f_n = \omega_n/2\pi$ of the oscillation (time function $cos(\omega_n t)$) and the shape of the object deformation (space function $\hat{z}_n(x)$), respectively . For a system solved by FEM with a finite number of degree of freedom, the number of modes solvable is also finite. It is important to note that only a lower range of eigenfrequencies have significant contribution to the time response of the whole system.

To assess the results of FEM solver, a rectangular beam was modelled and meshed with triangular elements [27]. The solver solves for mass, stiffness matrices and

20

eigenvalue problem (3.6). Parameters of the beam are as follow; $L = 1\text{m}$, $T = 0.2\text{m}$, $E = 10^6$ Pa and $\rho_s = 10^3 kg/m^3$. The beam was created using various mesh sizes, with the finest mesh up to $N = 700$. Figure 3.4 shows the mode shapes $\hat{z}_n$ of the first three oscillation modes (ie lowest three frequencies). The figures are showing good agreement with theoretical predictions and general outcome, by showing distinct series of n nodes (zero displacement) and n anti-nodes (maximum displacement) at specific locations along the beam.

Figure 3.5 shows the first two modes of eigenfrequencies f_n with respect to N, being the number of nodal points to mesh the beam. It shows fast convergence obtained with the increase of nodal points. The asymptotic value of f_1 and f_2 also in a very good agreement with the theoretical frequencies f_n^* predicted by (3.2).
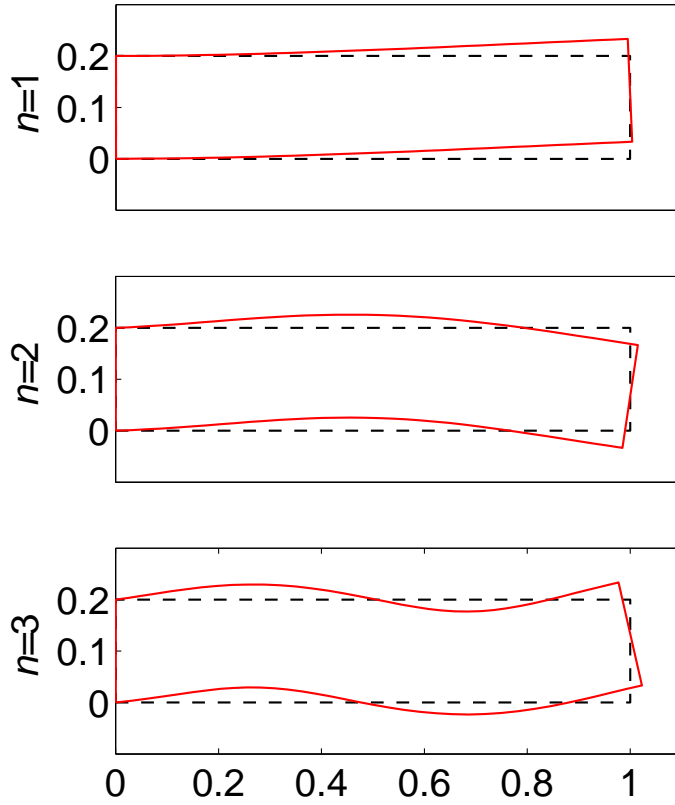
Figure 3.4: First three mode shapes of the free-oscillation of a beam clamped at one end
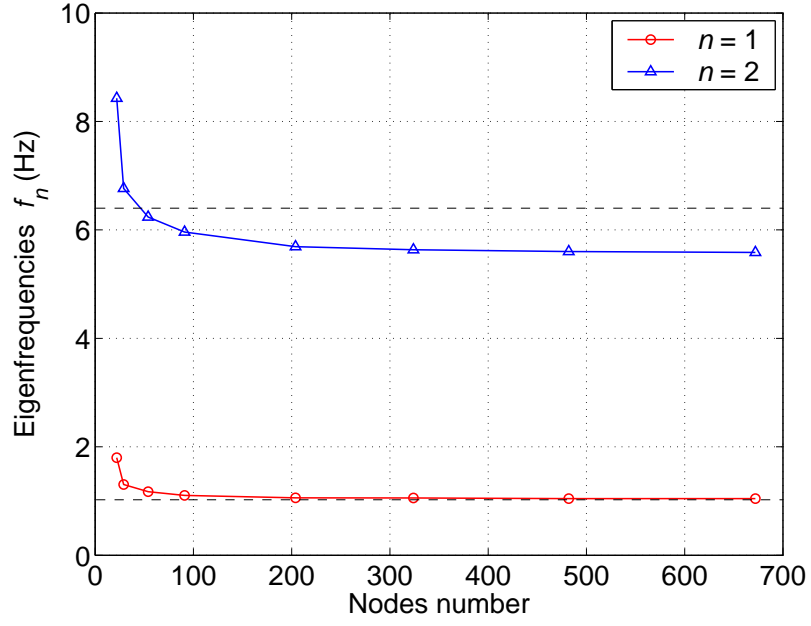
Figure 3.5: Lowest two eigenfrequencies of a beam clamped at one end

3.2.2 Volume Forces Implementation

For evaluation of volume force, a beam with a fixed end is considered and then placed in a gravitational field. From the elastic beam theory, the maximum vertical deflection due to gravitational field would be:

$$z_g^*(L) = \frac{3}{2} \frac{\rho_s g L^4}{E T^2} \tag{3.7}$$

where g is the gravitational acceleration. The same beam as in Section 3.2.1 was computed numerically by the FEM solver to find the deformation due to the gravitational field. FEM solver solved the static problem $Kz = F$, where the external force was applied as the volume force $f = \rho_s g$. Figure 3.6 shows the maximum vertical deflection with respect to number of nodal points N. The asymptotic value of $z_g(L)$ is within a very good agreement to theoretical value $z_g^*(L)$ as N increases, the error is less than 4% when $N = 482$.
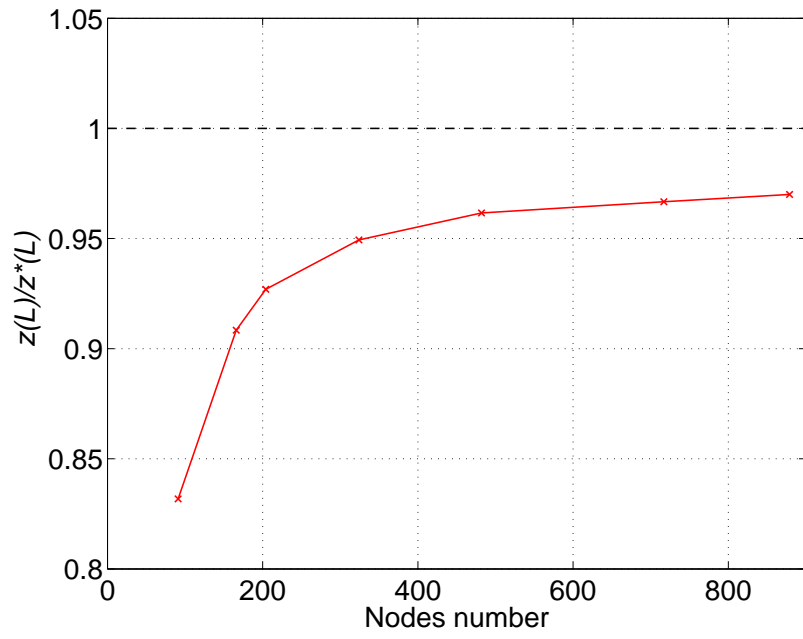
Figure 3.6: Maximum vertical deflection of a beam clamped at one end when gravitational field is applied

Chapter 4

Application of IBM-FEM with an Elastic Airfoil in a Uniform Flow

In this chapter, the IBM-FEM code is applied to an elastic airfoil in a uniform flow. Fluid and solid domains parameters are specified together with the boundary conditions. The airfoil is found to be oscillating when subjected to the uniform flow. The C_l, C_d curves are analyzed and compared to the frequencies of shedding vortices from the leading edge.

4.1 Numerical Setup

4.1.1 Computational Domain and Geometry

For the simulation involving IBM-FEM of an elastic airfoil in a uniform flow, the computational domain length and height are $10L$ and $7.5L$ respectively where L is the chord length of the airfoil as show in Figure 4.1. The airfoil is a NACA0012 symmetric airfoil. The leading edge of airfoil is located at $x = 2.5L$ from the inlet. On top and bottom boundaries of the computational domain, a periodic boundary condition is used. At the inlet, a constant velocity U_o is prescribed and at the outlet, gradient free condition is used.

4.1.2 Fluid and Solid Domain Parameters

Table 4.1 shows the fluid domain parameters used for the simulation of fluid-solid interaction by IBM and FEM. The Cartesian grid size, $\Delta x = \Delta y = 0.025$ with the
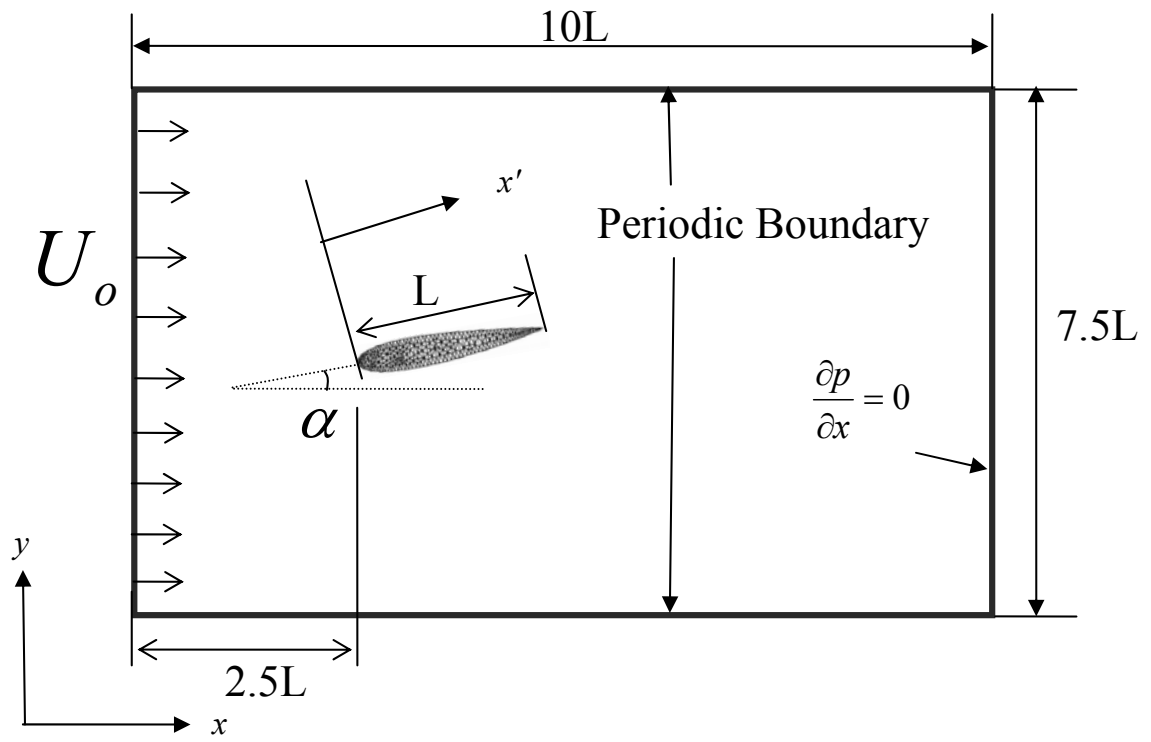
Figure 4.1: Schematics of computational domain

number of cells $n_x \times n_y = 400 \times 300$. The time step is $\Delta t = 0.003s$, the free stream velocity, $U_o = 1m/s$ and the Reynolds number, $Re = 500$.

Table 4.1: Fluid domain parameters

Number of grid point	n_x, n_y	400×300
Reynolds number	$Re \left(\frac{U_o L}{\nu}\right)$	500
Time increment	Δt	0.003
Grid size	$\Delta x, \Delta y$	0.025
Free stream velocity	U_o	1

Table 4.2 shows the solid domain parameters. The cases were setup between $-5°$ and $-10°$ angle of incidence. Two nodes located on the center line at $x'/L = 0.3$ and 0.4 are assigned as fixed points for the airfoil and the rest are free to deform. The airfoil is made of 456 triangular elements (n_e), with 293 total nodal points (n_p) generated using Triangle software [27]. A different set of material strength are considered for the airfoil with the properties given in Table 4.2.

Table 4.2: Solid domain parameters

Airfoil chord	L	1
Number of elements	n_e	456
Nodal points	n_p	293
Young's Modulus	E (Pa)	∞(Rigid), $5.0 \times 10^6, 2.0 \times 10^2, 1.0 \times 10^2$
Poisson Ratio	ν_s	0.45
Angle of incidence	α	-5° and -10°

4.1.3 Boundary Conditions

A constant uniform velocity $(u, v)_{x=0} = (U_o, 0)$ is prescribed at the inlet, while the convective boundary condition

$$\left(\frac{\partial \boldsymbol{u}}{\partial t} + \bar{u}\frac{\partial \boldsymbol{u}}{\partial x} \right)_{x=10L} = 0 \tag{4.1}$$

is specified at the outlet ($x = 10L$), where $\bar{u}$ is the mean convective velocity at the outlet. This is implemented on a collocated grid as

$$\boldsymbol{u}^{n+1}_{n_x+1,j} = \boldsymbol{u}^n_{n_x+1,j} - \bar{u}^n\frac{\Delta t}{\Delta x}(\boldsymbol{u}^n_{n_x+1,j} - \boldsymbol{u}^n_{n_x,j}) \tag{4.2}$$

where subscripts indicate space indices (i ranges from 0 to $n_x + 1$ and j from 0 to $n_y + 1$) and superscript indicate time indices (n stands for $t_n = n\Delta t$). The latter are omitted in some equations when all refer to the same time. The vector notation $\boldsymbol{u}$ is used when equations for u and v are the same. At the outlet a gradient-free condition is specified:

$$\left(\frac{\partial p}{\partial x} \right)_{x=10L} = 0 \tag{4.3}$$

and implemented as $p_{n_x+1,j} = \phi_{n_x,j}$. For top and bottom boundaries, periodic boundary conditions are specified.

4.2 Results and Discussion

4.2.1 Airfoil Oscillating in a Fluid Flow at $-5°$ Angle of Incidence

For airfoil at $-5°$ angle of incidence, Fig. 4.2 and 4.3 show the lift and drag coefficients in time history fashion for different Young's modulus values. For the enlarged section of the time history plot, the C_l and C_d were shown to be oscillating regularly. Three points of interest are marked on each C_l plot to represent the minimum, average and maximum down-force. At the exact time step, contour of absolute vorticity in the vicinity of the airfoil are are plotted and shown in Fig.4.4. For this plot, the Young's modulus is $E = 1.0 \times 10^2$ Pa. It is clear that the alternating vortex shedding are one of the contributing factor for oscillation in C_l and C_d with time. It shows the correlation between the vibrating nature of C_l and C_d with the edge displacement and vortex formation.

From the C_l and C_d plots, it is possible to calculate the frequencies of changes in lift and drag with time. Frequencies of the airfoil's trailing edge oscillation in the free
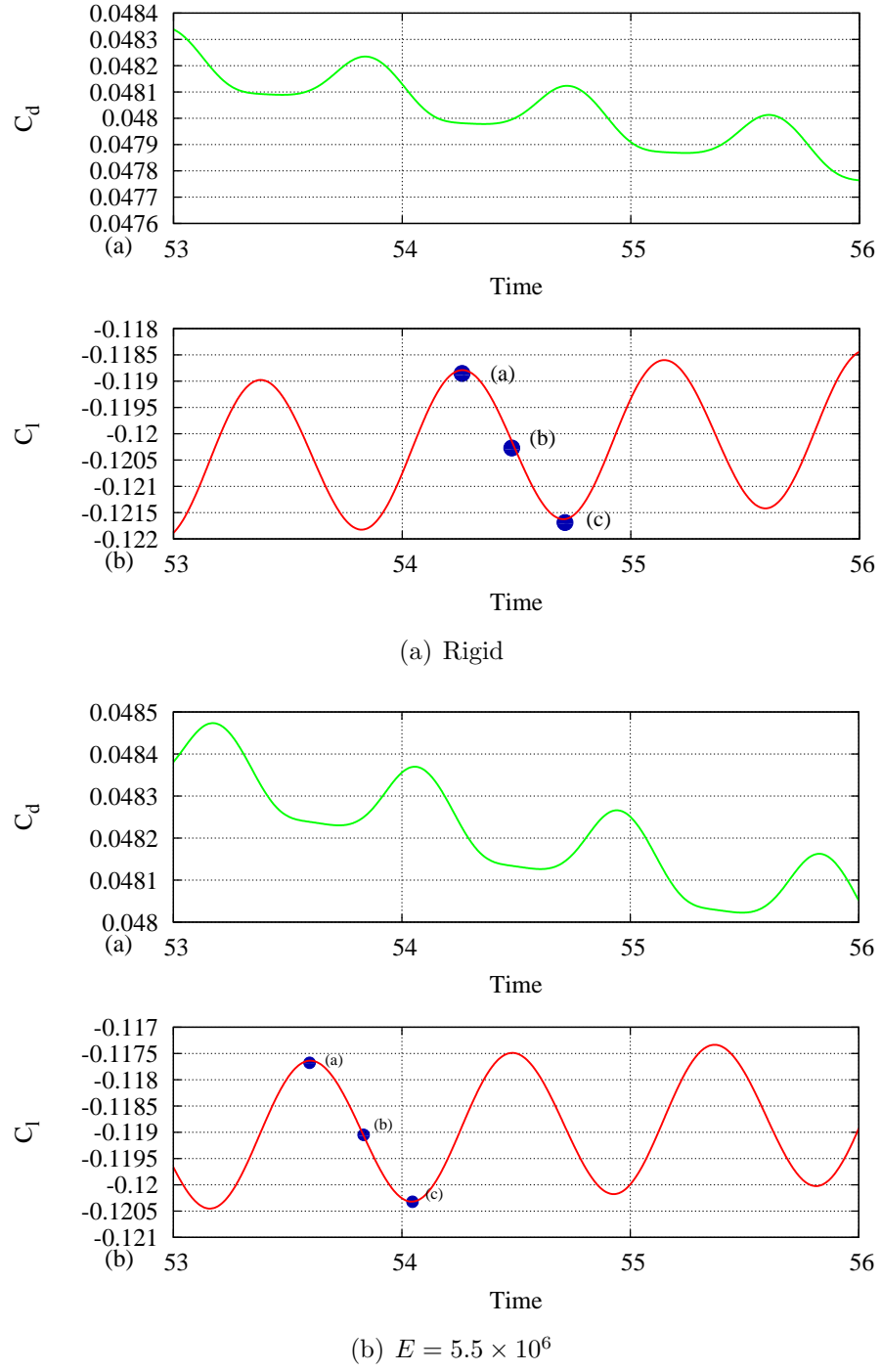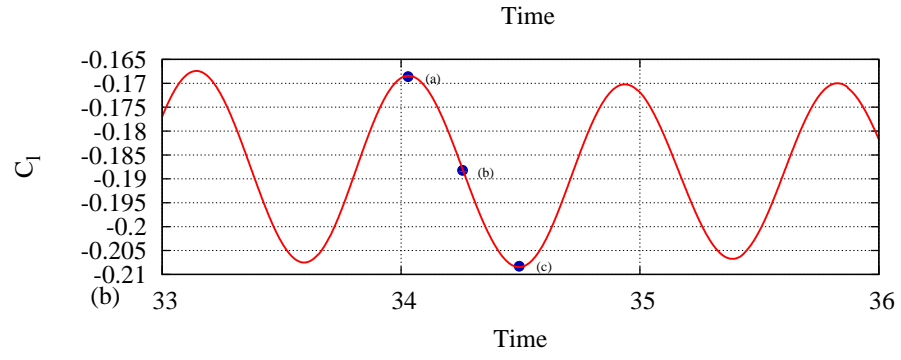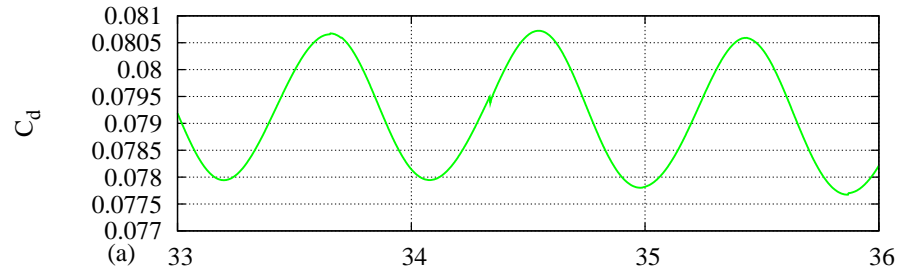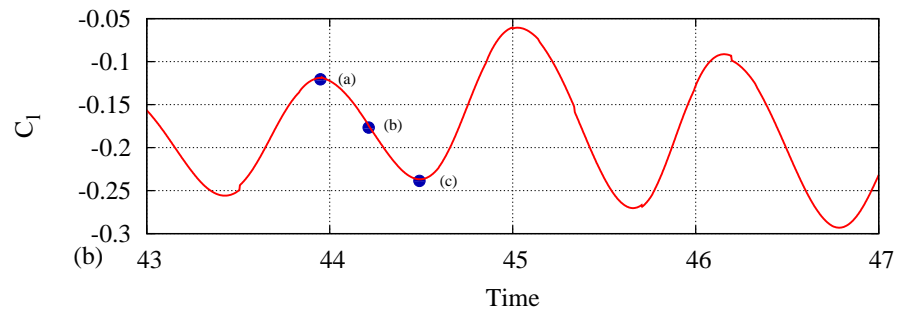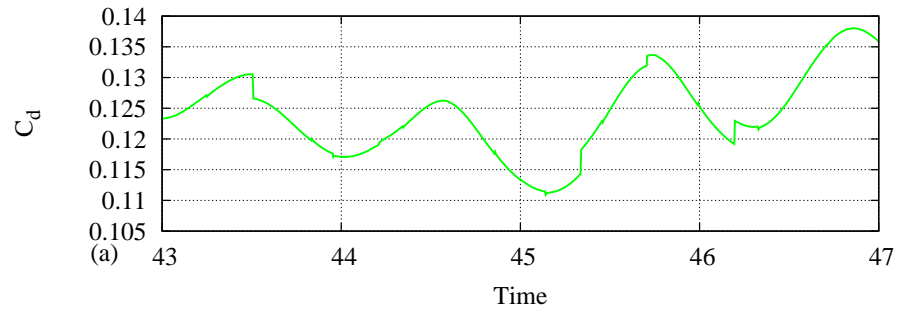
(a) Rigid

(b) $E = 5.5 \times 10^6$

Figure 4.2: Time history of lift and drag coefficient for airfoil at $-5°$ angle of incidence

(a) $E = 2.0 \times 10^2$

(b) $E = 1.0 \times 10^2$

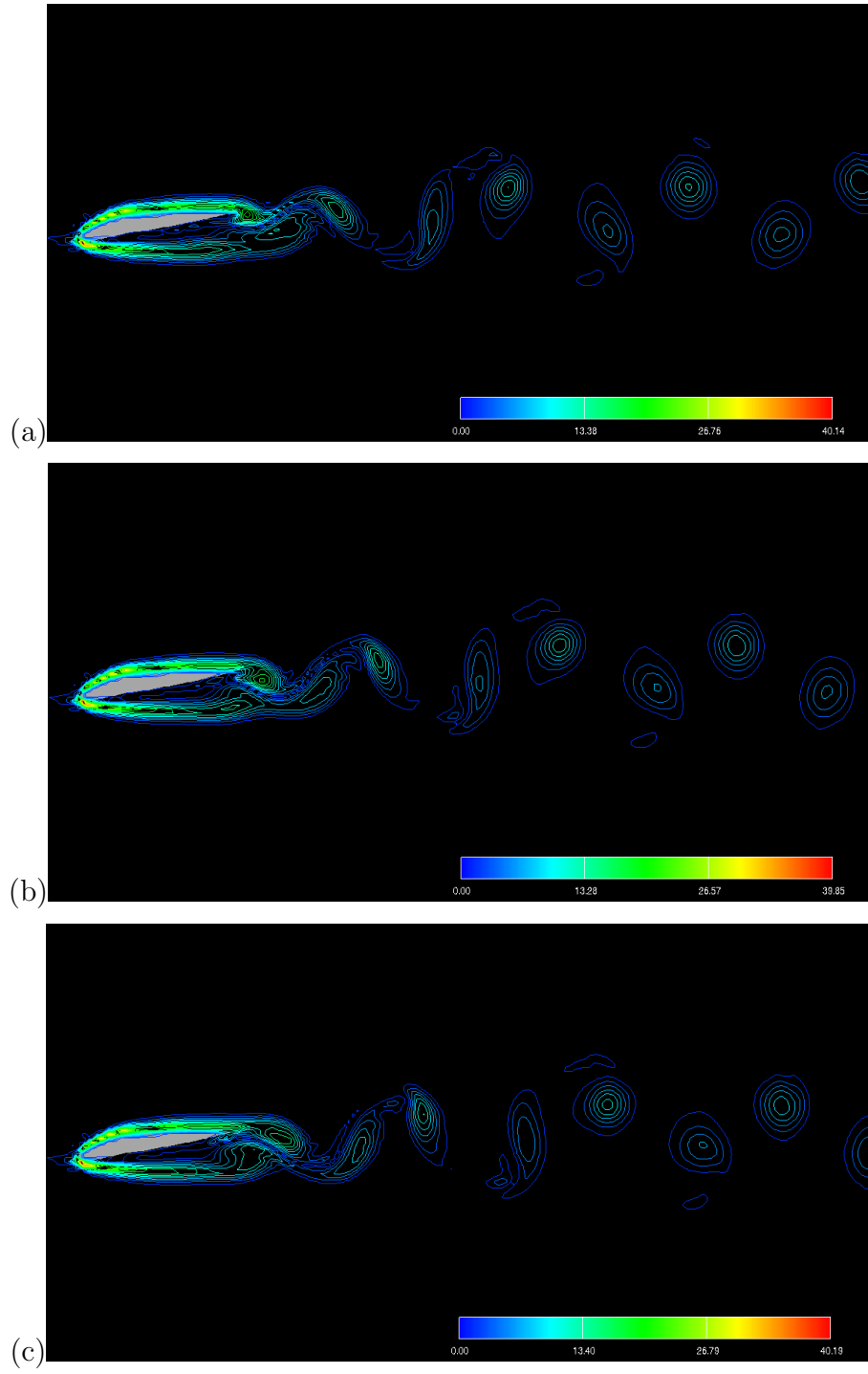Figure 4.3: Time history of lift and drag coefficient for airfoil at $-5°$ angle of incidence

29

Figure 4.4: Contours of absolute value of vorticity near the airfoil at $-5°$ angle of incidence, $E = 1.0 \times 10^2, Re = 500$ at:(a)minimum down-force;(b)average down-force;(c)maximum down-force

30

stream are also calculated. The eigenfrequency of the first mode are obtained from the FEM code. Table 4.3 shows the frequencies of C_l, trailing edge displacement and mode 1 of the airfoil. The C_l frequencies are proportional to the Young's modulus as the airfoil is getting softer, the frequency is also getting lower. Frequencies of the trailing edge also compares very well with the C_l. However, for Case III, the frequency is showing some possible discrepancies. The frequency is even higher than Case II which has higher E. Eigenfrequencies of the airfoil are totally in disagreement with values obtained for C_l and trailing edge.

Table 4.3: Frequencies of C_l and airfoil in free stream at $-5°$

Case	E	C_l Frequency	Trailing Edge Frequency	Eigenfrequency of Airfoil
	(Pa)	f(Hz)	f(Hz)	Mode 1, $f((Hz)$
I	∞ (Rigid)	1.136	-nil-	-nil-
II	5.5×10^6	1.124	1.124	3.483
III	2.0×10^2	1.099	1.16	0.0021
IV	1.0×10^2	0.926	0.926	0.0015

Figure 4.5 shows the plots of lift and drag coefficient of an airfoil ($E = 2 \times 10^2$ Pa) for the whole simulation time. When t is approaching $t = 60s$, it is clear that the lift is oscillating with a different mode. Prior to $t = 60s$, the oscillation is regular and better than the multimode oscillation. The irregularities in the oscillation could be due to numerical errors as no phase change was detected from the flow. However, there are also different factors that can cause this type of oscillation.

4.2.2 Airfoil Oscillating in a Fluid Flow at $-10°$ Angle of Incidence

For airfoil at $-10°$ angle of incidence, the results are following the trend of cases from $-5°$. Fig. 4.6 and 4.7 show the lift and drag coefficients in time history fashion for different Young's modulus values. Three points of interest are marked on each C_l plot to represent the minimum, average and maximum down-force. In these time steps, contour of absolute vorticity in the vicinity of the airfoil are plotted and shown in
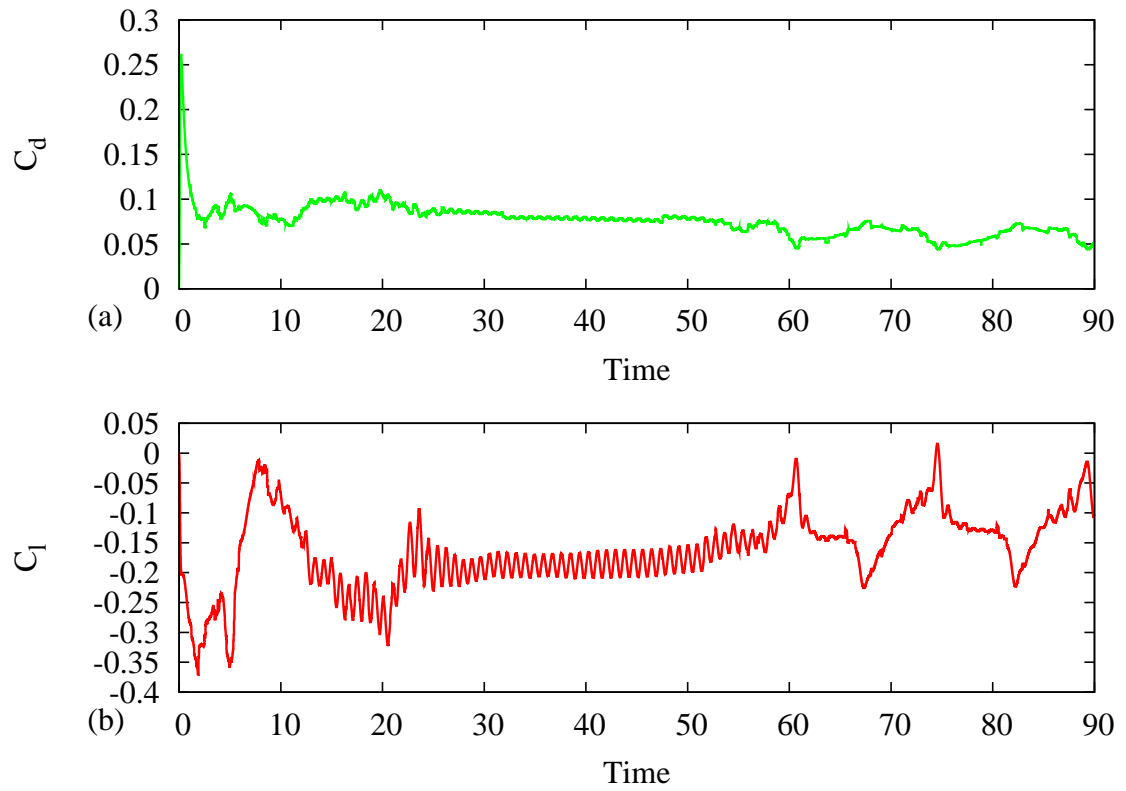
Figure 4.5: Time history of lift and drag coefficient for airfoil ($E = 2 \times 10^2$) at $-5°$ angle of incidence

Fig.4.8. For this plot, the Young's modulus is $E = 1.0 \times 10^2$ Pa. It is clear that the alternating vortex shedding is one of the contributing factors for oscillation in C_l and C_d with time.

Table 4.4 shows the frequencies of C_l and trailing edge displacement. Contrary to $-5°$ case, it remains true that C_l frequencies are proportional to the Young's modulus ie.: as the airfoil is getting softer, the frequency is also getting lower with the frequencies of the trailing edge, also agreeing to the C_l frequencies. For comparison with eigenfrequencies, the results are again in total disagreement.

Figure 4.9 shows the plots of lift and drag coefficient for the whole simulation time. This time, the plots are showing the multiple mode shapes experienced by the airfoil. The oscillation happens very early in the simulation, on the contrary to the $-5°$.

Table 4.4: Frequencies of C_l and airfoil in free stream at $-10°$

Case	E	C_l Frequency	Trailing Edge Frequency	Eigenfrequency of Airfoil
	(Pa)	f(Hz)	f(Hz)	Mode 1, f(Hz)
I	∞ (Rigid)	1.053	-nil-	-nil-
II	5.5×10^6	1.042	1.052	3.483
III	2.0×10^2	0.862	1.0	0.0021
IV	1.0×10^2	0.769	0.64	0.0015

4.2.3   Discussion

Real fluid-solid interaction is highly complicated in nature, such simple representation in this study is not enough to provide full physical understanding. From the results in Table 4.3 and 4.4, we can see there is a general tendency that when the Young's Modulus (E) is lower, the trailing edge oscillation frequecies is also smaller. This is in line with the reduction of eigenfrequencies of the airfoil with softer airfoil. With more samples, we can deduce that the trailing edge frequencies are directly proportional to the strength of the material.

Figure 4.5 and 4.9 show strong nonlinear vibration of C_l and C_d with respect
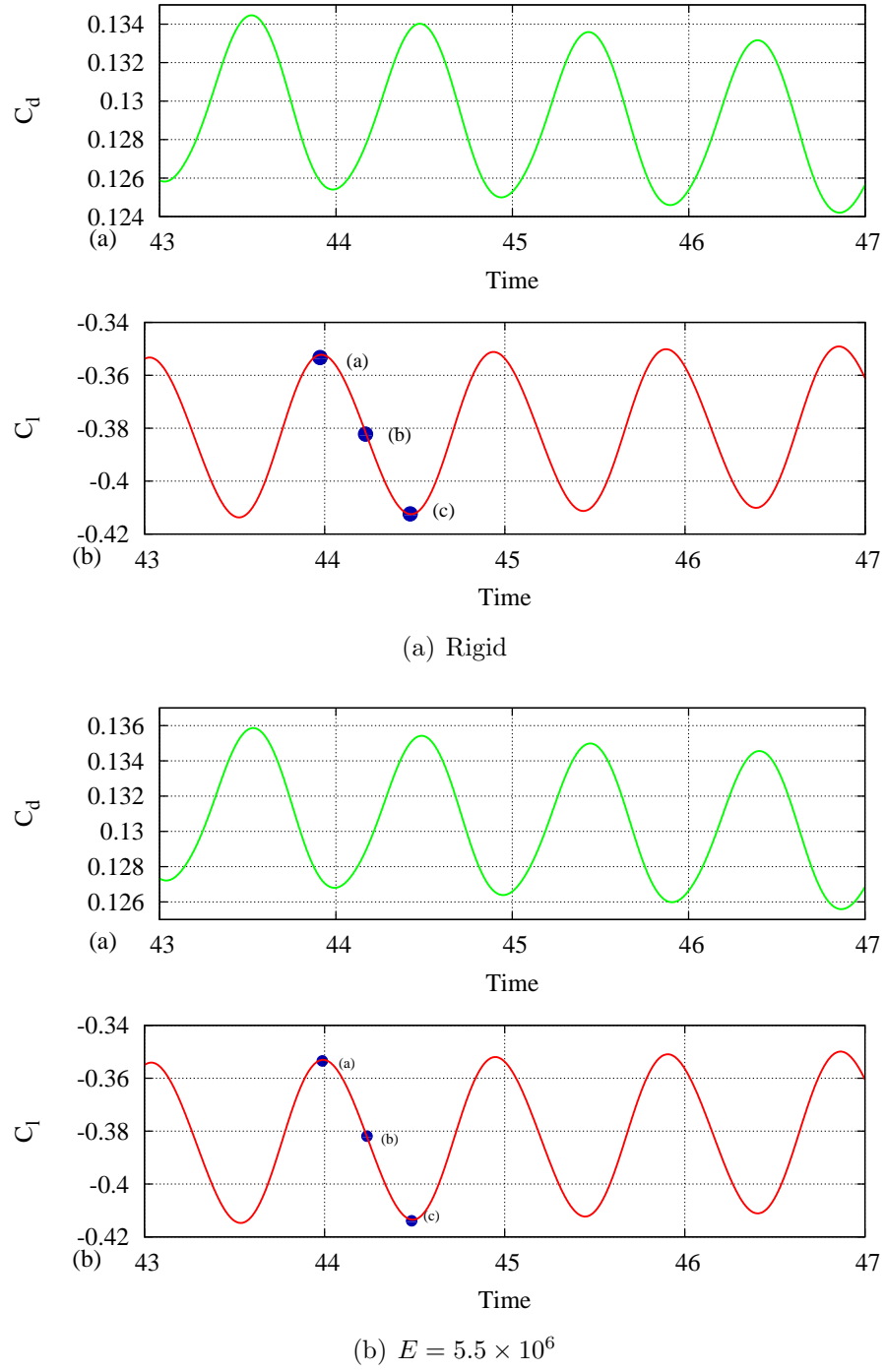
(a) Rigid

(b) $E = 5.5 \times 10^6$

Figure 4.6: Time history of lift and drag coefficient for airfoil at $-10°$ angle of incidence
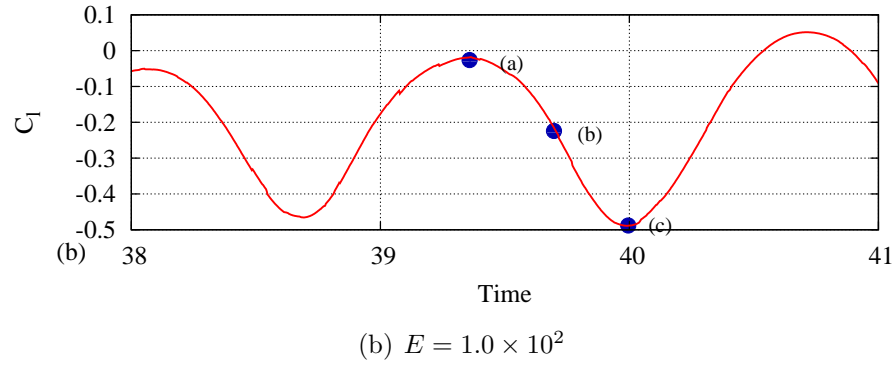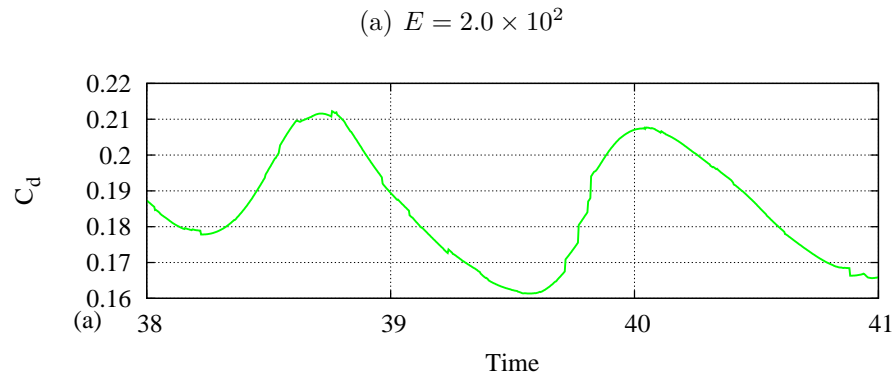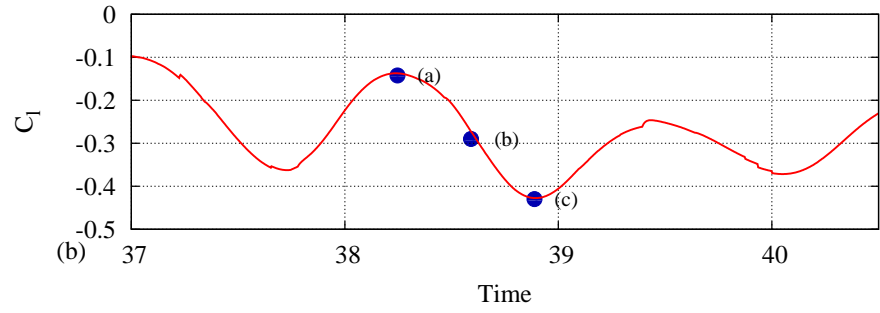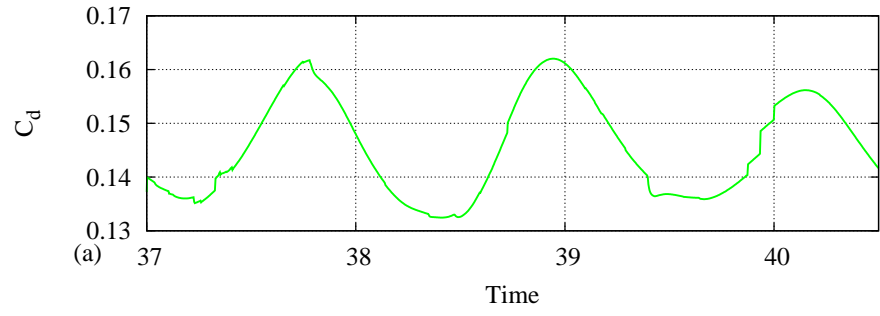
(a) $E = 2.0 \times 10^2$

(b) $E = 1.0 \times 10^2$

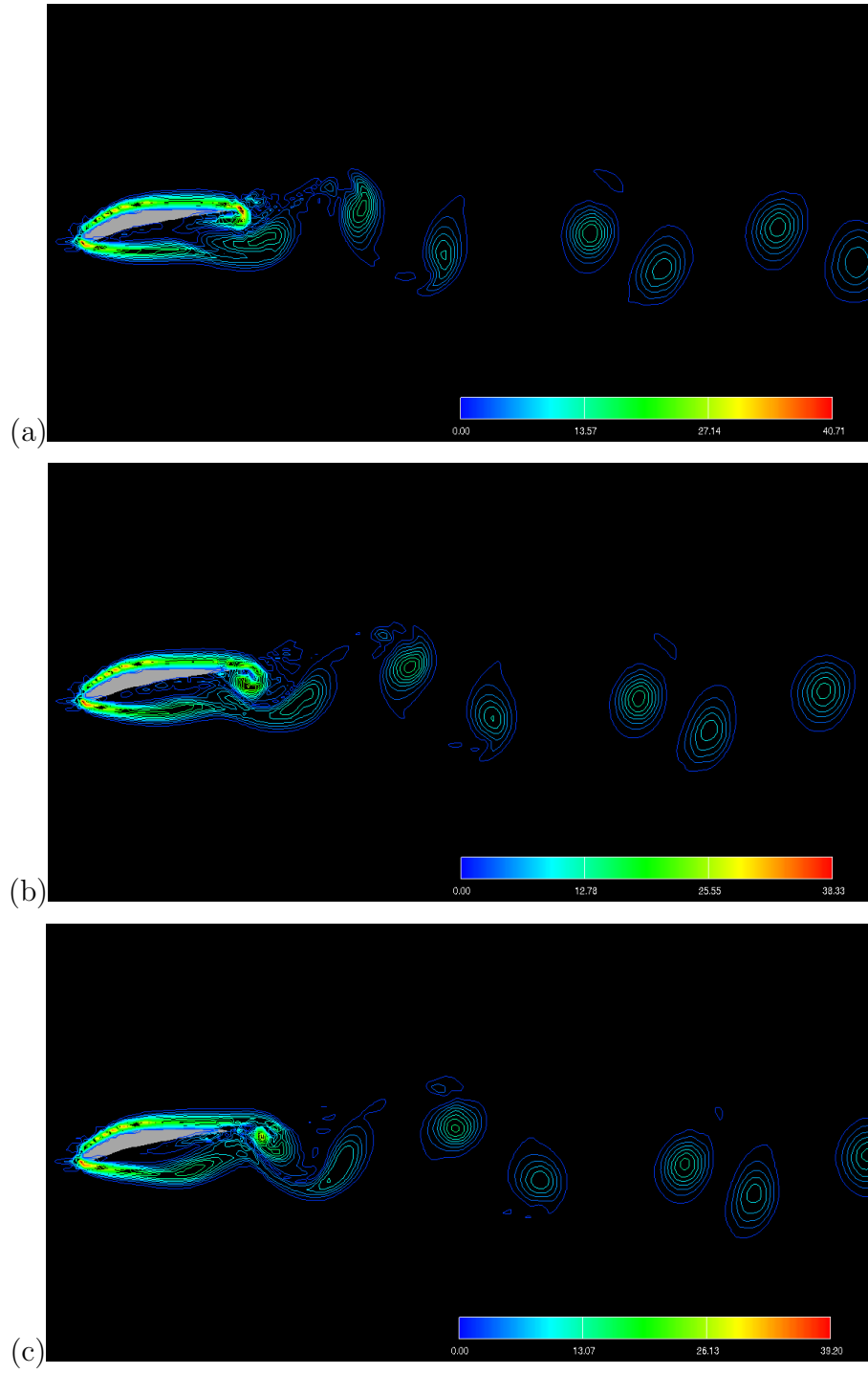Figure 4.7: Time history of lift and drag coefficient for airfoil at $-10°$ angle of incidence

Figure 4.8: Contours of absolute value of vorticity near the airfoil at $-10°$ angle of incidence, $E = 1.0 \times 10^2, Re = 500$ at:(a)minimum down-force;(b)average down-force;(c)maximum down-force
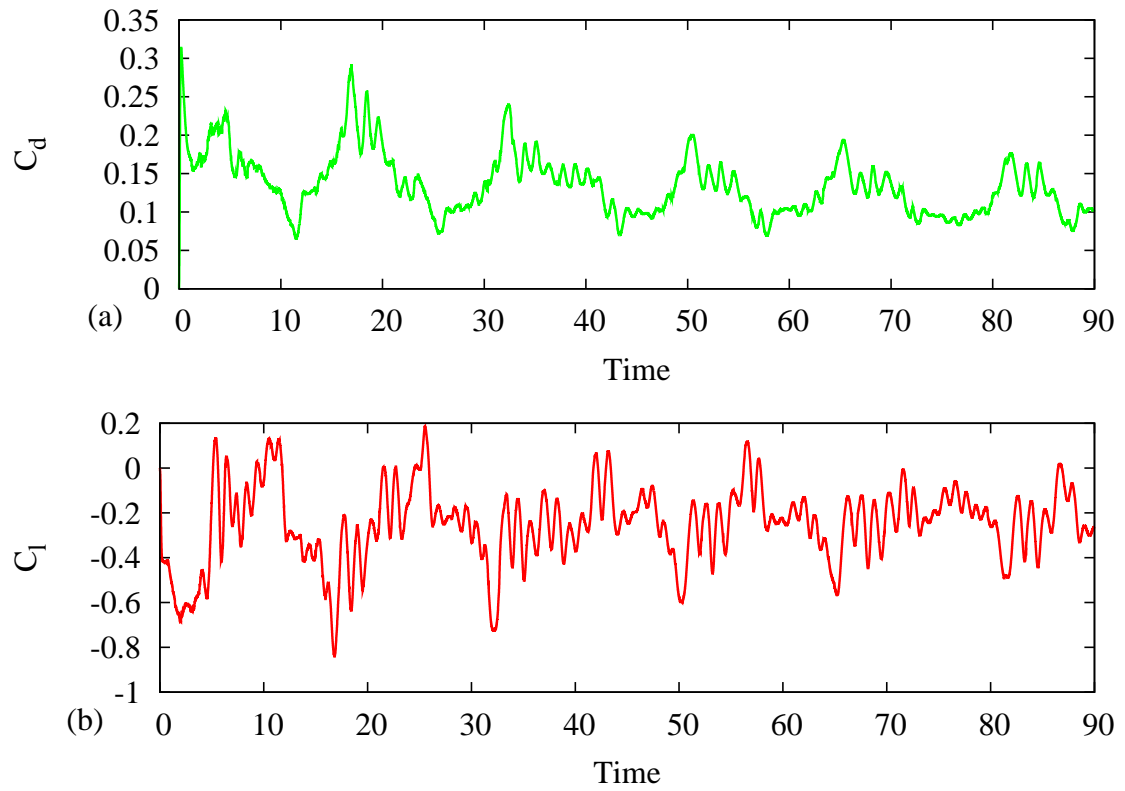
Figure 4.9: Time history of lift and drag coefficient for airfoil ($E = 2 \times 10^2$) at $-10°$ angle of incidence

to time. Few causes might influence the vibration, eg. multimode vibration of the airfoil, strong interaction between fluid and solid and also numerical error if the wave shape is very erratic. Multimode vibration usually caused by different forcing function acting at the same time on the object. Numerical error causes the derivation of C_l and C_d to be inconsistent as the value fluctuates hence giving a very nonlinear graph. This nonlinearity is more apparent at very low E which suggested that it can be one of the reason for such results. As we are observing the trends of the lift and drag coefficients, further investigation is required to accurately understand the real nature of the events. Also it is again recommended to find the link between eigenfrequencies and the frequencies of C_l and vortex shedding.

Chapter 5

Conclusion

In the present study, a new fluid-structure interaction (FSI) approach using IBM-FEM to solve the interaction of incompressible viscous fluid and an elastic body was proposed. Kajishima's [17] method was used to define the boundary of the structure and derive the velocity field near the elastic body, and the pressure field was solved using fractional step method. An efficient pressure retrieval method is also developed for the fluid-structure coupling, which would significantly reduce the number of cells needed to be scanned. Second-stage velocity and pressure corrections were proposed to take into account the effect of momentum exchange on the pressure field. Pressure and viscous force were used as surface forces on the elastic body and the deformation solved by FEM. The chapters can be summerized as follows:

- IBM was validated by obtaining the C_p distribution on the airfoil. Meanwhile, FEM was validated through calculation of eigenfrequencies and deflection due to gravity.

- Using pressure and viscous force as fluid-structure coupling, it was successfully applied for fluid flow past an elastic deformable body. Mixed modes in the vibration of the airfoil were clearly observed, especially when the Young's modulus is 1.0×10^2 Pa.

- For a moderately stiff airfoil, the oscillation shows very close agreement with the generation of vortex at the trailing edge.

- Reducing the strength of the material is resulting the decrease the frequency of the trailing edge.

This study shows the applicability of the proposed method in simulating fluid-solid interaction problems. The method is able to simulate a strong interaction between fluid and solid. This method can be further expanded into various applications such as in biology, heart valves and blood flow, solid mechanics and aeroelasticity.

List of Publication

Papers in Scientific Journal

1. Tuan-Ya T.M.Y.S., Takeuchi S. and Kajishima T. and Ueyama A.,"Immersed boundary method (body force) for flow around thin bodies with sharp edges"; International Journal of Mechanical and Materials Engineering (accepted).

Presentation at International and Domestic Conference

1. Boujo E., Tuan-Ya T.M.Y.S., Takeuchi S., Kajishima T., "Study of fluid-structure interaction problem involving deformable objects by a new finite element - immersed boundary approach."3rd International Symposium on Aero Aqua Bio-Mechanisms, Np.P07(CD), July 2006, Ginowan, Okinawa, Japan.

2. Tuan-Ya T.M.Y.S.,Takeuchi S. and Kajishima T.,"Study of hydrodynamic force acting on an elastic object using immersed boundary and finite element methods"; Symposium on Computational Fluid Dynamics, NO.B5-4(CD); December 2006; Nagoya, JAPAN.

3. Tuan-Ya T.M.Y.S.,Takeuchi S. and Kajishima T.,"Immersed boundary and finite element methods approach for interaction of an elastic body and fluid by two-stage correction of velocity and pressure"; Proc. Joint ASME-JSME Fluids Engineering Conference, FEDSM2007-37160(CD); July 2007; San Diego, California, USA.

4. Tuan-Ya T.M.Y.S.,Takeuchi S. and Kajishima T.,"Immersed boundary method for flow around thin bodies with sharp edges", 3rd Asian-Pacific Congress on Computational Methods, p.28 (abstract), December 2007, Kyoto, JAPAN

Appendix A

IBM for Thin Profile Object

To apply IBM (body force) on a thin profile object, a new method is developed to identify surrounding fluid cells nearest to the Lagrangian point on the object's surface. For each node on the surface of the object, the method selects a 3×3-mesh around the cell to which the node belongs. The same procedure is repeated for all nodes and redundant cells will be removed. Local solid volumetric fraction of each cells are calculated using Equations (2.14,2.15,2.16). Since the thin object has 2-sides, 1 side must be treated as an external surface and another side as internal surface. Figure A.1 shows the selected fluid cells near the thin body.

A.1 Simulation Setup

Two simulation cases have been set up. Case 1, involving a crescent shaped thin body and Case 2 with thin airfoil. Both bodies are initially placed in a fluid at rest and the thin airfoil with an attack angle of 15°. The fluid is subjected with an instantaneous start at the inlet with velocity U_o. Figure A.2 and A.3 show schematics of the computational domains for both cases and Table A.1 and A.2 shows the computational conditions. On top and bottom boundaries, a periodic boundary condition is used. At the inlet, a constant velocity is prescribed and at the outlet, a gradient free condition is used.
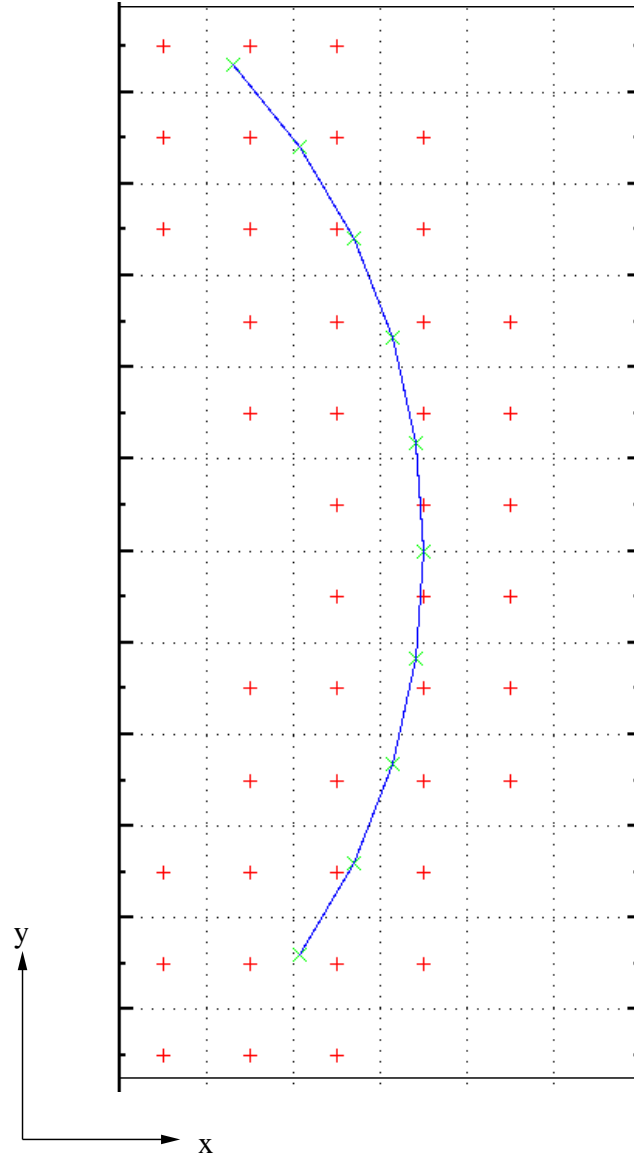
Figure A.1: Fluid cells selected for calculation of local volumetric fraction

43

Table A.1: Computational setup for crescent shaped body (case 1)

Parameters	Coarse mesh	Fine mesh
Number of grid point	200×150	400×300
Reynolds number, $Re\left(\frac{U_oL}{\nu}\right)$	200	200
Time increment, Δt	0.005	0.0025
Grid size,$\Delta x, \Delta y$	0.1	0.05

Table A.2: Computational setup for this airfoil (case 2)

Parameters	Coarse mesh	Fine mesh	Extra fine mesh
Number of grid point	200×150	400×300	800×600
Reynolds number, $Re\left(\frac{U_oL}{\nu}\right)$	200	200	200
Time increment, Δt	0.005	0.0025	0.00125
Grid size,$\Delta x, \Delta y$	0.1	0.05	0.025
Angle of attack (α)	15°	15°	15°
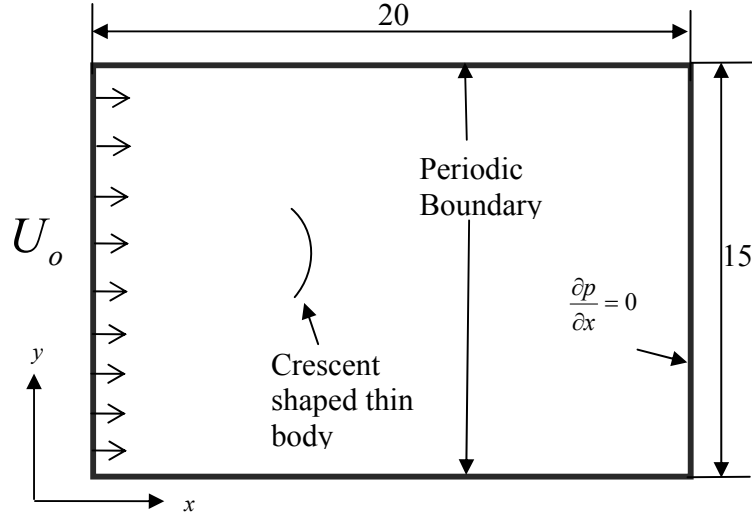
Figure A.2: Schematic of computational domain for crescent shaped thin body
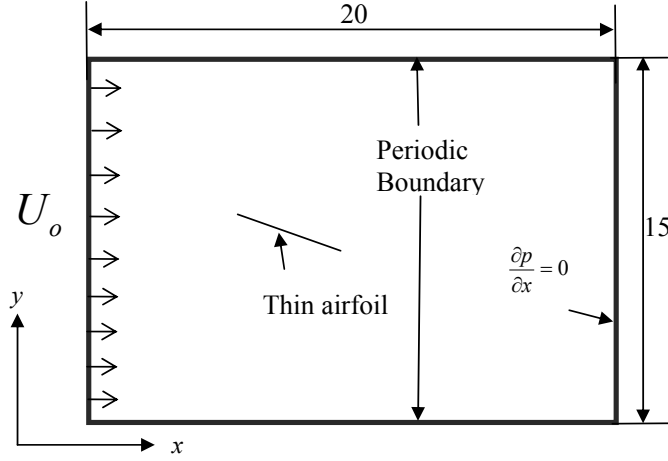
Figure A.3: Schematic of computational domain for thin airfoil

A.2 Results and Discussion

A.2.1 Crescent shaped thin body

For a crescent shaped thin body, two possible configurations were tested for the selection of further mesh refinement. The first configuration is to assign the surface facing the incoming flow as the external surface (left external) and the second configuration assigns the surface opposing the incoming flow as the external surface (right external). Figure A.4 shows the velocity vectors for both configurations. The plots are at the same time instance of $t = 5$ where the flow is still developing. From the plots, we can observe the virtual thickness represented by the empty spaces. From there, we can see that the configuration of LE is much better in simulating the flow over a thin body.

The virtual thickness area is identified as an area that needs to be handled to obtain a reasonable solution. Further refinement of the mesh is done to see the effect on the virtual thickness. Figure A.5 shows the velocity vectors for the refined mesh of a crescent shaped thin body. Figure A.5(a) plotted at the instance of $t = 5$ where the fluid flow is still developing and Figure A.5(b) plotted at $t = 200$ where the fluid flow is fully developed. The virtual thickness area seems to be reduced quite significantly. With further refinement, the virtual thickness will become negligible to the dimension of the thin body.
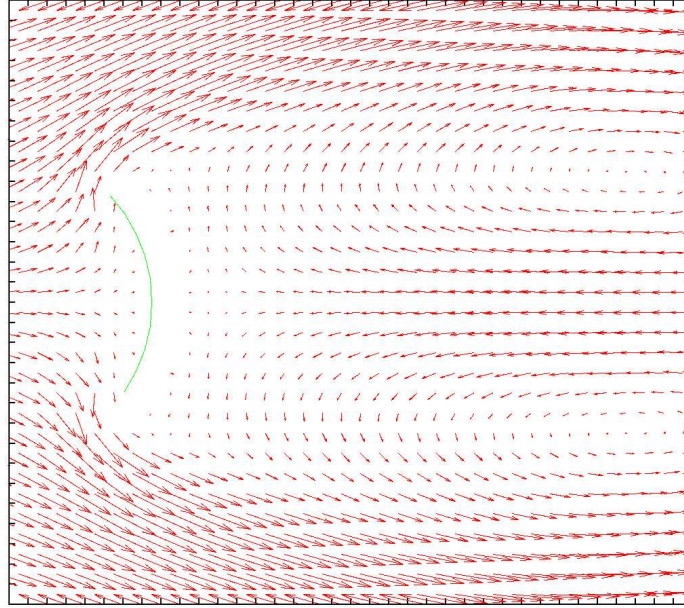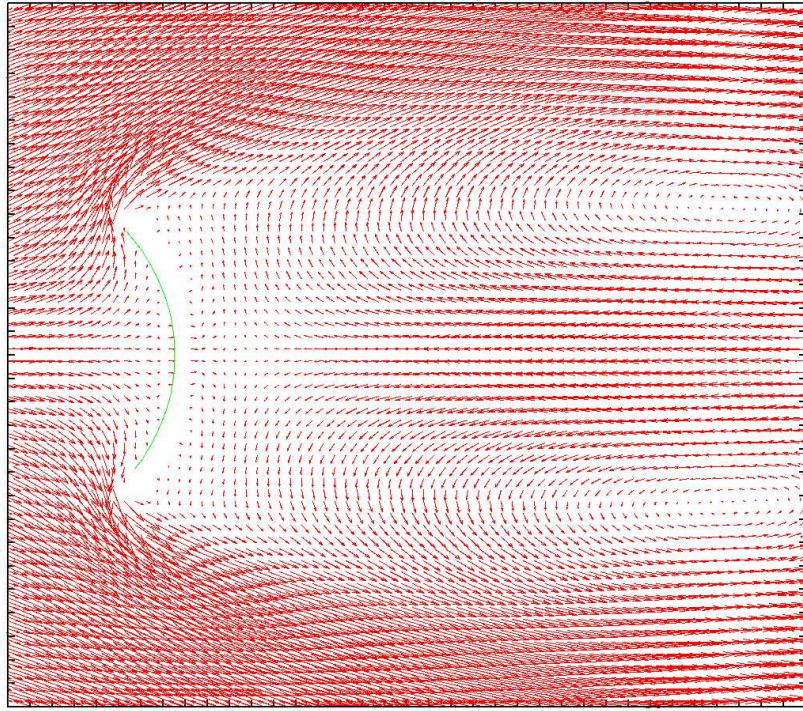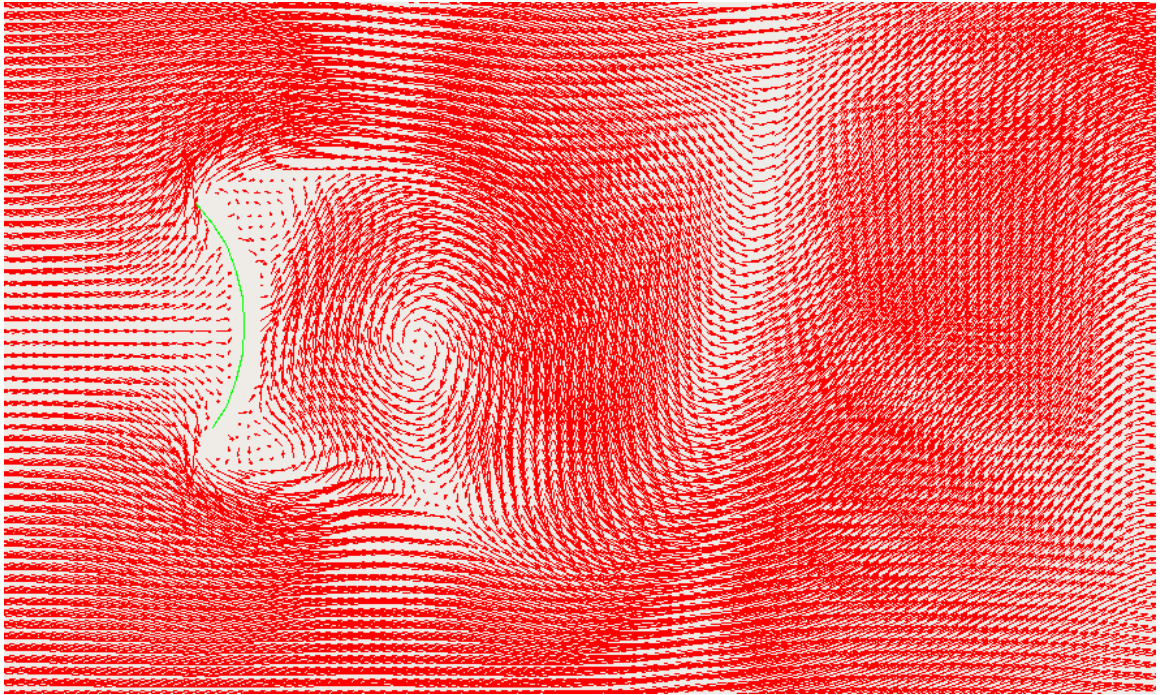
(a) Left external (LE)
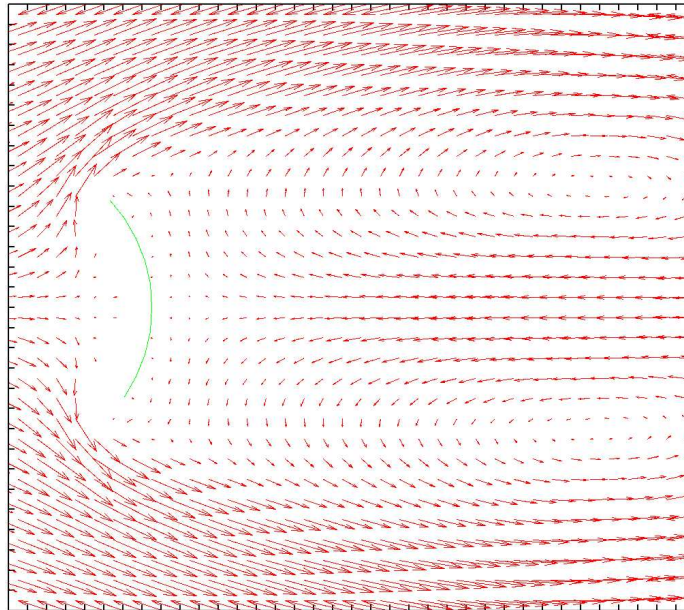
(b) Right external (RE)

Figure A.4: Velocity vectors plot for LE and RE on crescent shaped thin body at the same time instance of $t = 5$

(a) At time instance of $t = 5$

(b) At time instance of $t = 200$

Figure A.5: Velocity vector plot of refined mesh for crescent shaped thin body

A.2.2 Thin airfoil

To study the effect of mesh refinement on the virtual thickness, thin airfoil is subjected under the same flow condition as a crescent shaped thin body. The mesh was refined up to 3 times and the coefficient of lift is measured for all three instances. Figure A.6 shows the velocity vectors of flow around thin airfoil with 3 mesh sizes. In Figure A.6(a), the velocity vectors clearly show the effect of virtual thickness as the flow near the leading edge is being deflected quite significantly. Refinement of mesh shows the reduction of deflection due to virtual thickness of the thin airfoil.

(a) Coarse mesh

(b) Fine mesh
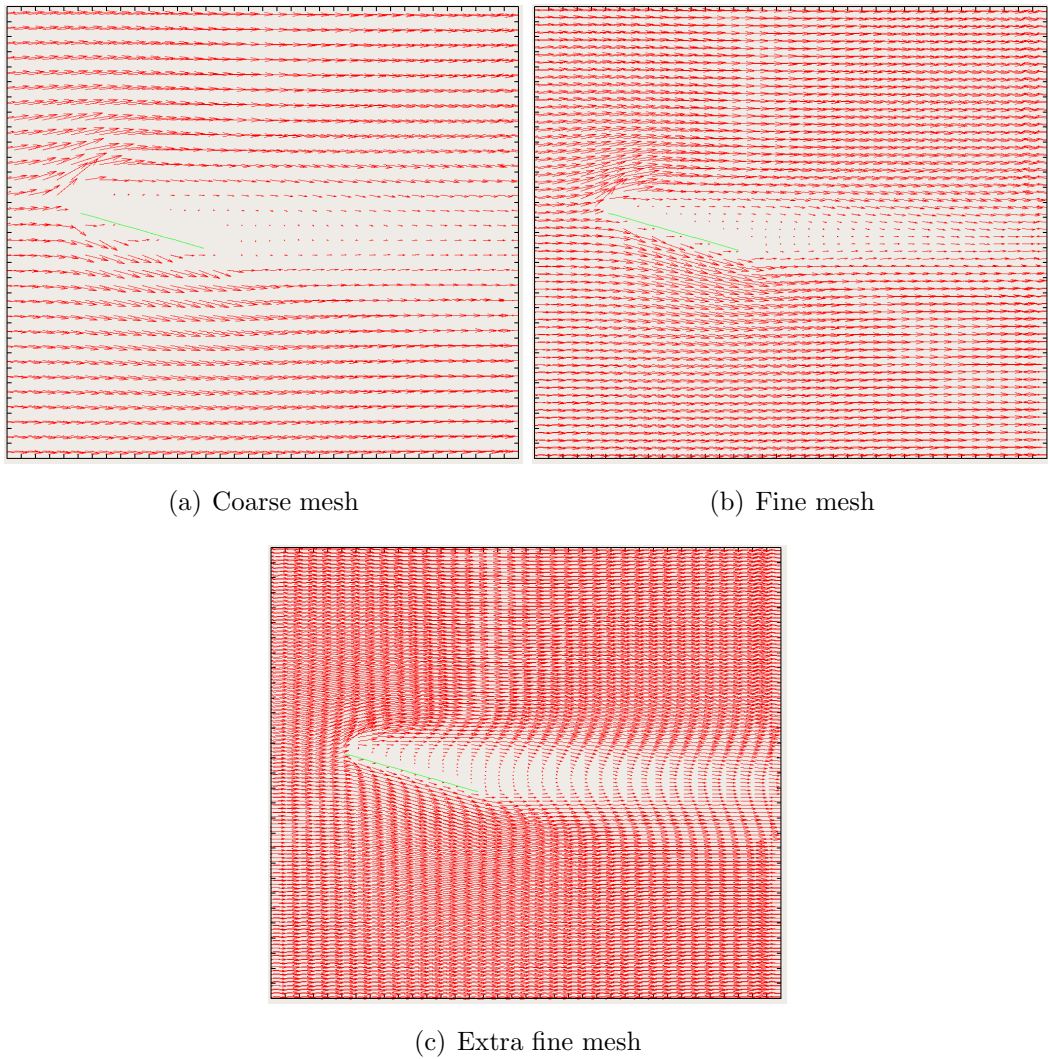
(c) Extra fine mesh

Figure A.6: Velocity vectors of thin airfoil with 3 different mesh sizes

Table A.3 shows the C_L of thin airfoils with 3 different mesh sizes. C_L for fine and extra fine mesh are very close in values. It shows the convergence in C_L with respect to mesh refinement. The virtual thickness for fine meshes is negligible such that, it does not affect much in the values of C_L.

Table A.3: C_L of thin airfoil according to mesh sizes

Mesh size, Δx	C_L
0.1	0.84
0.05	0.74
0.025	0.75

Appendix B

Airfoil and Mesh Construction

B.1 NACA Profile

The undeformed airfoil shape is based on NACA 0012 profile which belongs to NACA 4-digit series. It was designed for aircaft wings and developed by National Advisory Committee for Aeronautics (NACA). The airfoil shape can be precisely generated by equations that described the properties. Equation B.1 is for generating NACA 0012.

$$\pm y = 0.6(0.29\sqrt{x} - 0.1260x - 0.3516x^2 + 0.2843x^3 - 0.1015x^4 \tag{B.1}$$

The NACA 4-digit series can be defined as:

- First digit describing the maximum camber as percentage of the chord.

- Second digit describing the distance of maximum camber from the airfoil leading edge in tens of percent of the chord.

- Last two digits describing maximum thickness of the airfoil as percent of the chord.

Therefore, the NACA 0012 airfoil is symmetrical, the 00 indicating it has no camber and has a maximum thickness of 12% of the chord.

B.2 Meshing with Triangle Software

The coordinates of NACA 0012 can be generated by Equation B.1 or obtained from various sources such as handbooks or internet. The completed airfoil profile can be

meshed Triangle software [27]. Triangle is a C program for two-dimensional mesh generation and construction of Delaunay triangulations, constrained Delaunay triangulation and Voronoi diagrams. Some of the command line switches that are used in meshing the airfoil are:

- `-p` meshes an input file (.poly file) which contains a collection of vertices and segments that describe line, holes and attributes;

- `-r` refines a previously generated mesh.

- `-q` quality mesh generation with no angles is smaller than 20°. Another minimum value can be specified as such as `-q28`. However in practical, the algorithm will succeed for minimum angle up to 30° but could not converge for angle above 34°;

Appendix C

Wilson-θ Method

Wilson-θ is an implicit method for solving equations or systems of equations in step by step manner, such as the second-order equations of motion (2.25) and (2.29). It was earlier developed to overcome stiff problems in finite element analysis.

Wilson-θ assumed that the acceleration varies linearly over time interval $I = [t_n; t_n + \theta \Delta t]$ where θ is a constant. Following the assumption, the acceleration at any time $t = t_n + \tau$ is:

$$\ddot{z}_{n+\tau} = \ddot{z}_n + \frac{\tau}{\theta \Delta t}(\ddot{z}_{n+\theta} - \ddot{z}_n) \tag{C.1}$$

Integrating Equation C.1 for velocity and displacement at instant $t_n + \tau$:

$$\dot{z}_{n+\tau} = \dot{z}_n + \tau \ddot{z}_n + \frac{\tau^2}{2\theta \Delta t}(\ddot{z}_{n+\theta} - \ddot{z}_n) \tag{C.2}$$

$$z_{n+\tau} = z_n + \tau \dot{z}_n + \frac{\tau^2}{2}\ddot{z}_n + \frac{\tau^3}{6\theta \Delta t}(\ddot{z}_{n+\theta} - \ddot{z}_n) \tag{C.3}$$

Substituting $\tau = \theta \Delta t$ into (C.3) produces the acceleration at instant of $t = t_n + \theta \Delta t$:

$$\ddot{z}_{n+\theta} = \frac{6}{(\theta \Delta t)^2}(z_{n+\theta} - z_n) - \frac{6}{\theta \Delta t}\dot{z}_n - 2\ddot{z}_n \tag{C.4}$$

Solving (C.2) and (C.4) gives the velocity:

$$\dot{z}_{n+\theta} = \frac{3}{\theta \Delta t}(z_{n+\theta} - z_n) - 2\dot{z}_n - \frac{\theta \Delta t}{2}\ddot{z}_n \tag{C.5}$$

Finally, by substituting Equations (C.4) and (C.5) into equation of motion (2.29) produces:

$$\left(K + \frac{3}{\theta\Delta t}C + \frac{6}{(\theta\Delta t)^2}M\right) z_{n+\theta} = F_{n+\theta} + C\left(\frac{\theta\Delta t}{2}\ddot{z}_n + 2\dot{z}_n + \frac{3}{\theta\Delta t}z_n\right)$$
$$+ M\left(2\ddot{z}_n + \frac{6}{\theta\Delta t}\dot{z}_n + \frac{6}{(\theta\Delta t)^2}z_n\right) \tag{C.6}$$

therefore the displacement $z_{n+\theta}$ can be calculated, provided the state $\{z_n, \dot{z}_n, \ddot{z}_n\}$ at instant t_n is known and Equation (C.4) is inverted. Finally, the desired condition of $\{z_{n+1}, \dot{z}_{n+1}, \ddot{z}_{n+1}\}$ at instant $t_n + \Delta t$ is obtained from Equations (C.1)-(C.3) where τ is replaced by Δt.

Whenever the damping matrix is represented as a linear combination of the mass and stiffness matrices, such as Equation (2.30), $C = f_m M + f_k K$, then C does not need to be calculated, and Equation (C.6) can be rewritten as:

$$\left[\left(1 + \frac{3f_k}{\theta\Delta t}\right)K + \left(\frac{6}{(\theta\Delta t)^2} + \frac{3f_m}{\theta\Delta t}\right)M\right] z_{n+\theta}$$
$$= F_{n+\theta} + K\left[\frac{f_k\theta\Delta t}{2}\ddot{z}_n + 2f_k\dot{z}_n + \frac{3f_k}{\theta\Delta t}z_n\right] \tag{C.7}$$
$$+ M\left[\left(2 + \frac{f_m\theta\Delta t}{2}\right)\ddot{z}_n + \left(\frac{6}{\theta\Delta t} + 2f_m\right)\dot{z}_n + \left(\frac{6}{(\theta\Delta t)^2} + \frac{3f_m}{\theta\Delta t}\right)z_n\right]$$

Wilson-θ method is unconditionally stable if $\theta > 1.37$. However, large value of θ may cause unnatural damping, and the value $\theta = 1.4$ is mostly recommended.

Appendix D

Figures of C_l, C_d and Contours of Absolute Vorticity

The figures presenting the C_l, C_d and the contours of absolute vorticity are presented for each cases simulated in this study. C_l and C_d are presented in time history graph in order to capture the effect of vortex formation with the values of lift and drag. The time histories plots are first shown over the whole simulation time and a section is selected for further magnification. From the magnified figures, corresponding minimum, average and maximum downforce are identified from C_l curve. For each points selected, a corresponding absolute vorticity contours is produced. From here, the relevance of C_l can be deduced with the formation of vortex structures.

D.1   5° cases
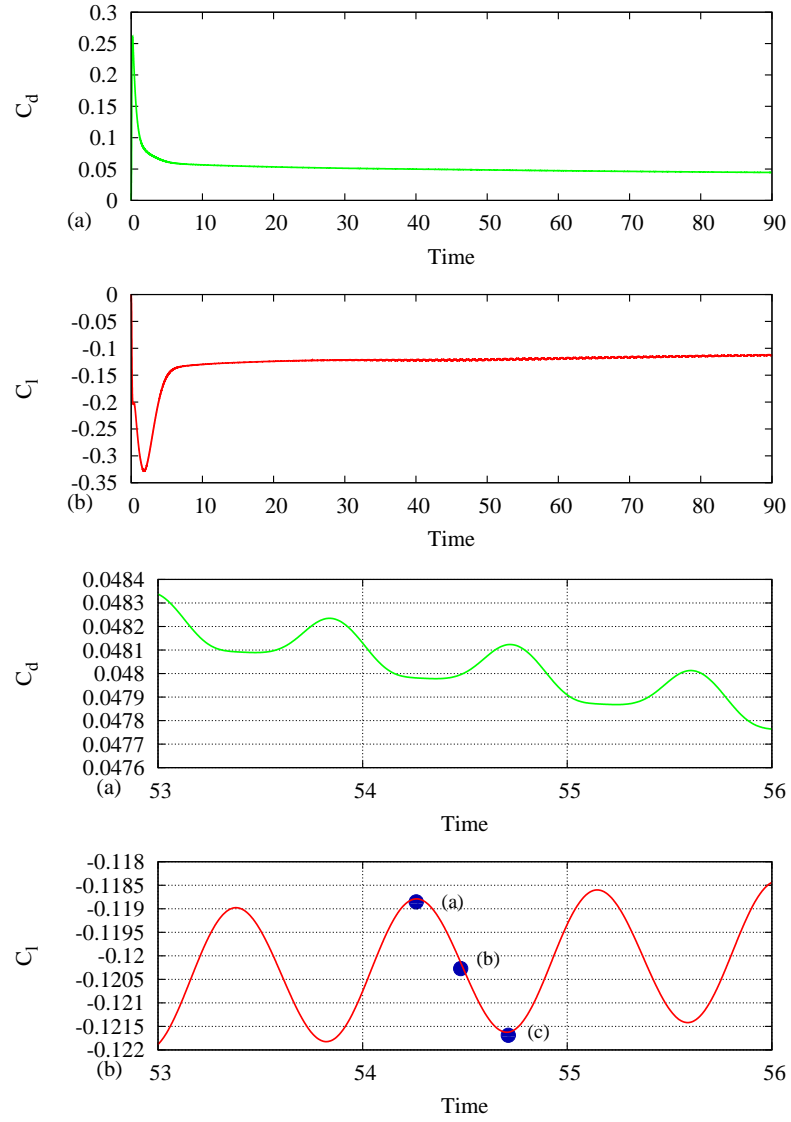
Figure D.1: Time history of lift and drag coefficient for rigid airfoil at $-5°$ angle of incidence:(a)minimum downforce;(b)average downforce;(c)maximum downforce
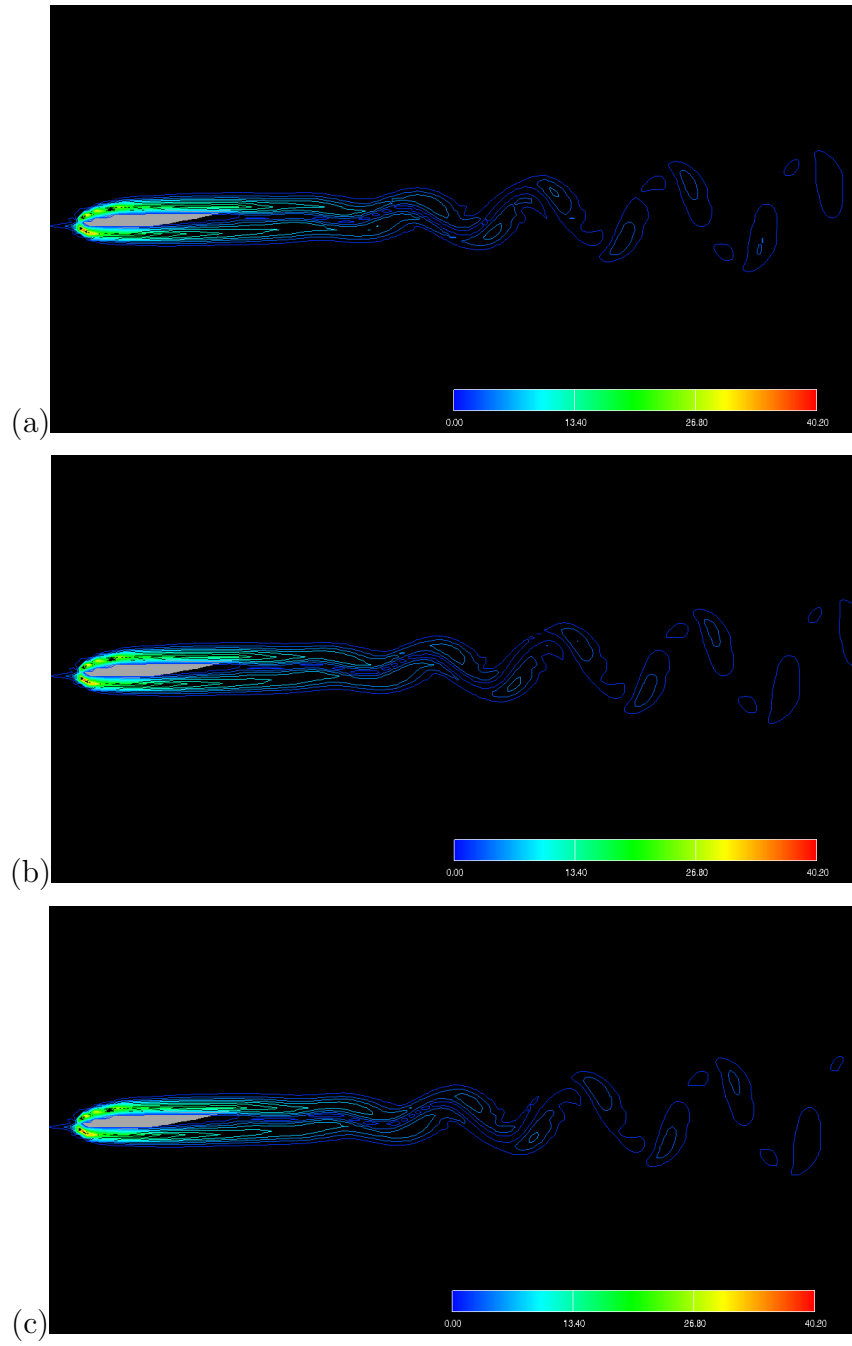
Figure D.2: Contours of absolute value of vorticity near the rigid airfoil at $-5°$ angle of incidence at:(a)minimum downforce;(b)average downforce;(c)maximum downforce
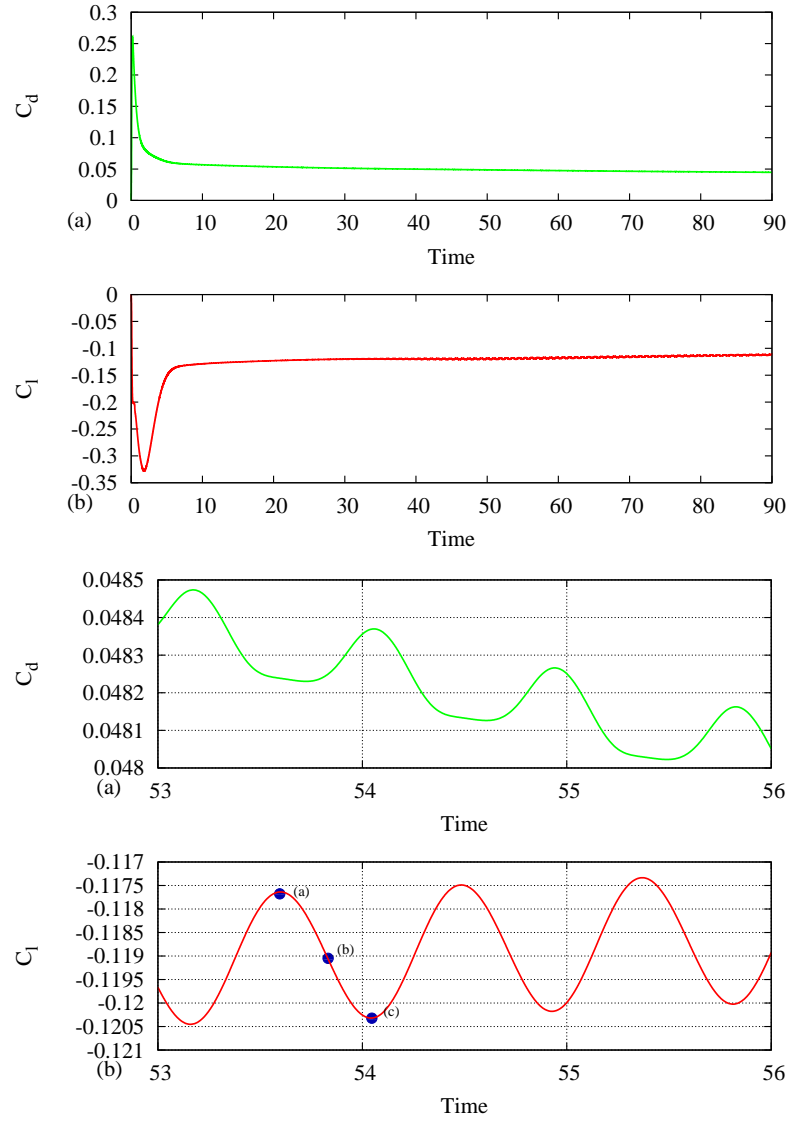
Figure D.3: Time history of lift and drag coefficient for airfoil ($E = 5.5 \times 10^6$ Pa) at $-5°$ angle of incidence:(a)minimum downforce;(b)average downforce;(c)maximum downforce
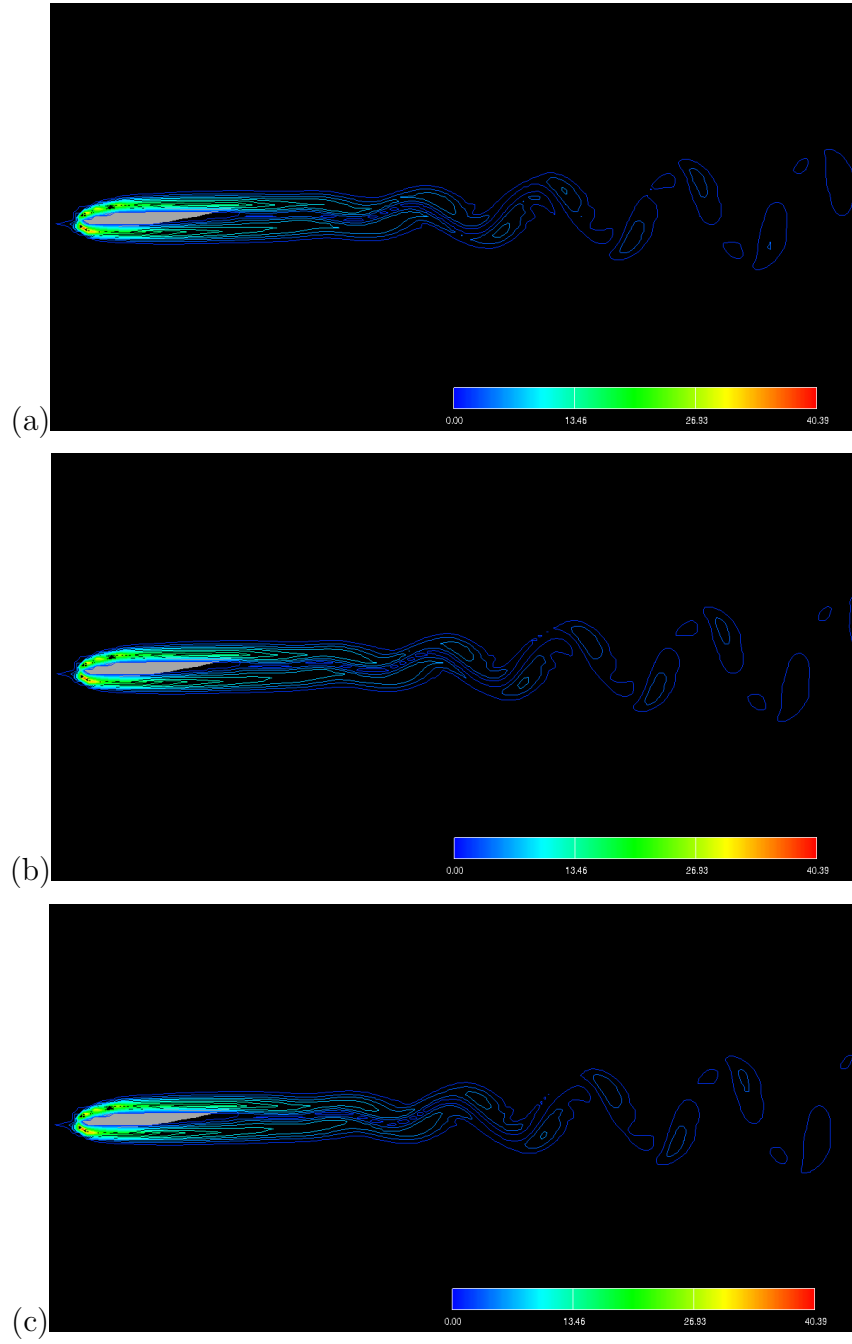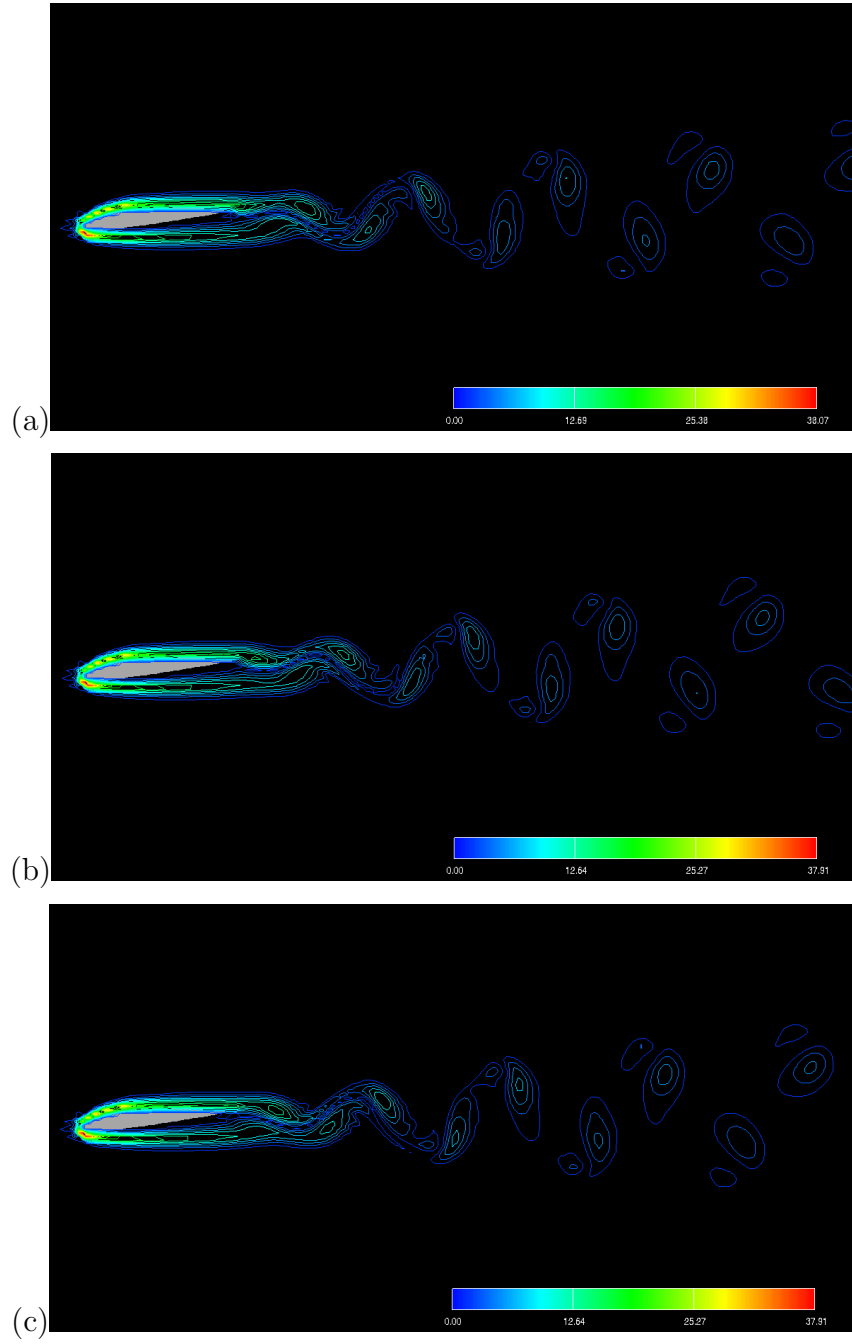
Figure D.4: Contours of absolute value of vorticity near the airfoil ($E = 5.5 \times 10^6$ Pa) at $-5°$ angle of incidence at:(a)minimum downforce;(b)average downforce; (c)maximum downforce
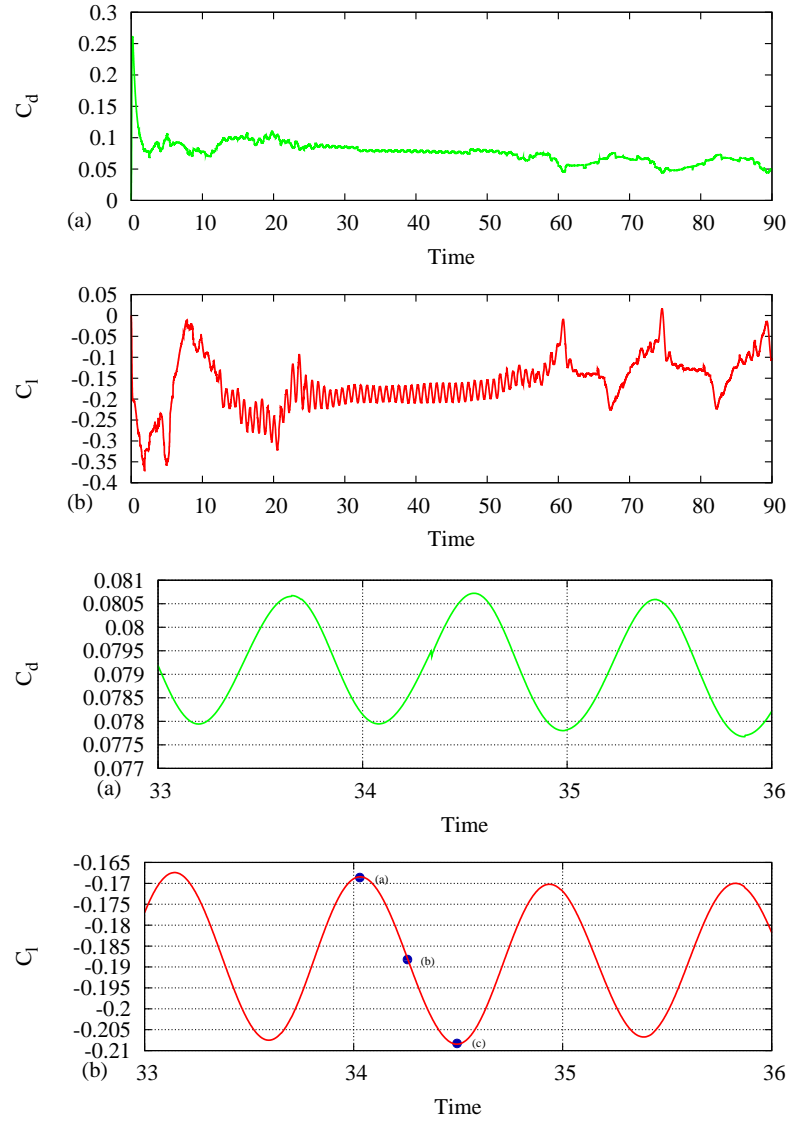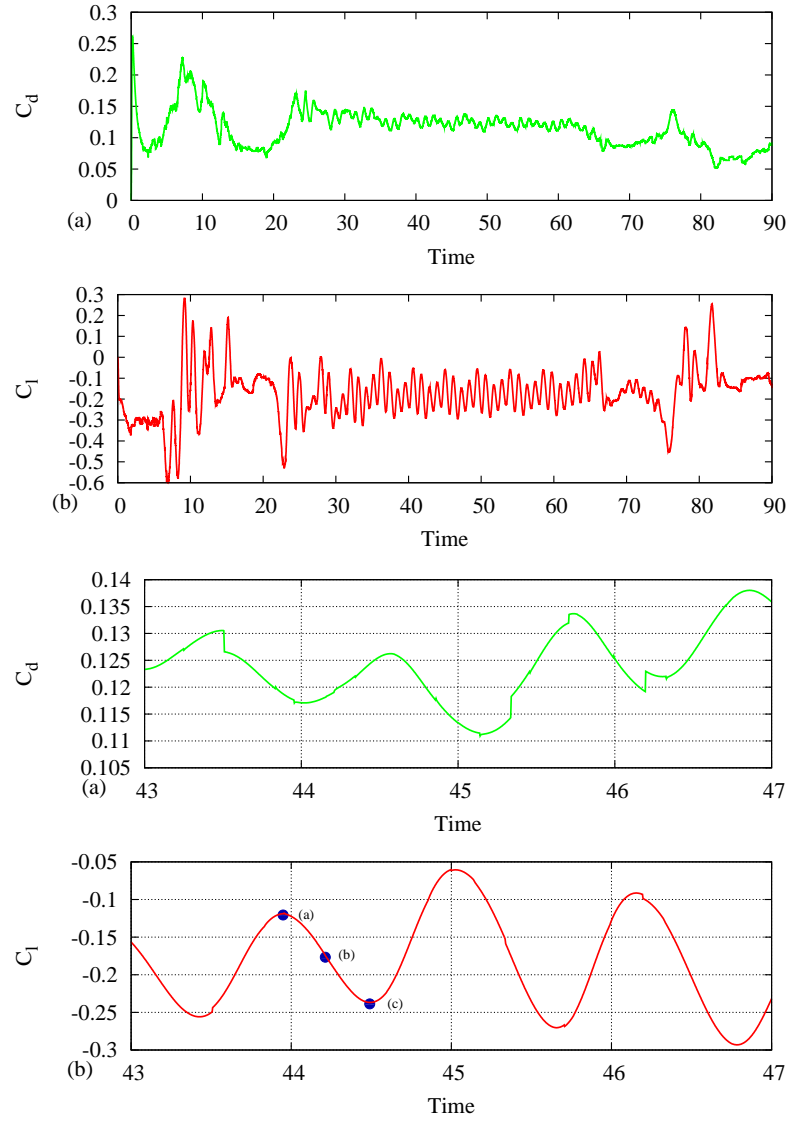
Figure D.5: Time history of lift and drag coefficient for airfoil ($E = 2.0 \times 10^2$ Pa) at $-5°$ angle of incidence:(a)minimum downforce;(b)average downforce;(c)maximum downforce
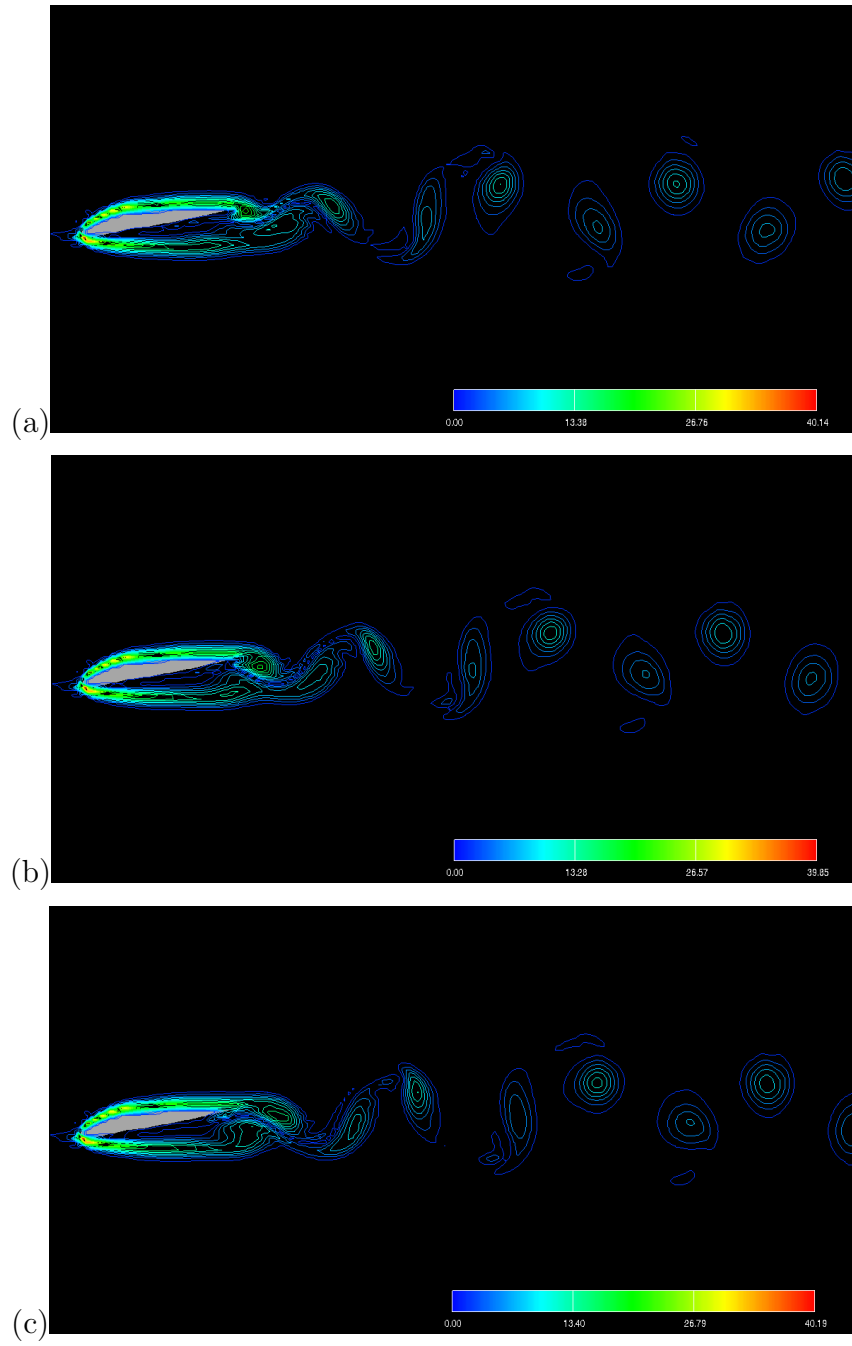
59

Figure D.6: Contours of absolute value of vorticity near the airfoil ($E = 2.0 \times 10^2$ Pa) at $-5°$ angle of incidence at:(a)minimum downforce;(b)average downforce;(c)maximum downforce

Figure D.7: Time history of lift and drag coefficient for airfoil ($E = 1.0 \times 10^2$ Pa) at $-5°$ angle of incidence:(a)minimum downforce;(b)average downforce;(c)maximum downforce

Figure D.8: Contours of absolute value of vorticity near the airfoil ($E = 1.0 \times 10^2$ Pa) at $-5°$ angle of incidence at:(a)minimum downforce;(b)average downforce;(c)maximum downforce
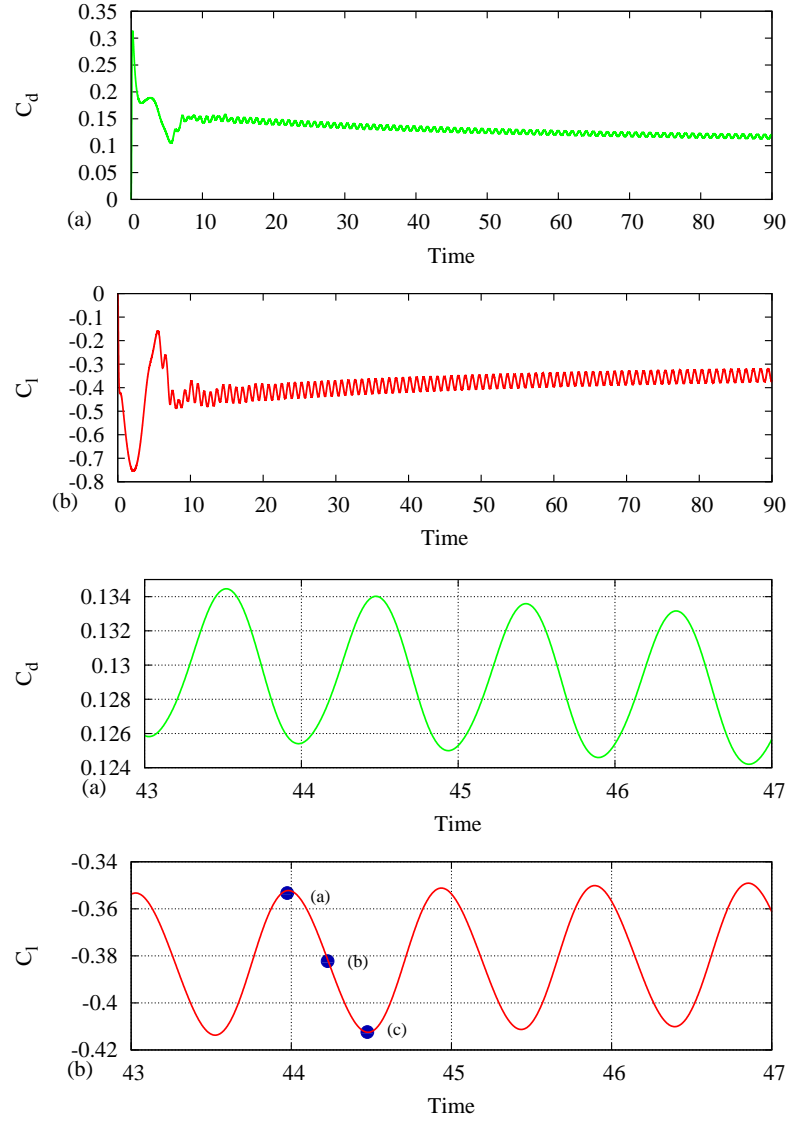
D.2 $10°$ cases

Figure D.9: Time history of lift and drag coefficient for rigid airfoil at $-10°$ angle of incidence:(a)minimum downforce;(b)average downforce;(c)maximum downforce
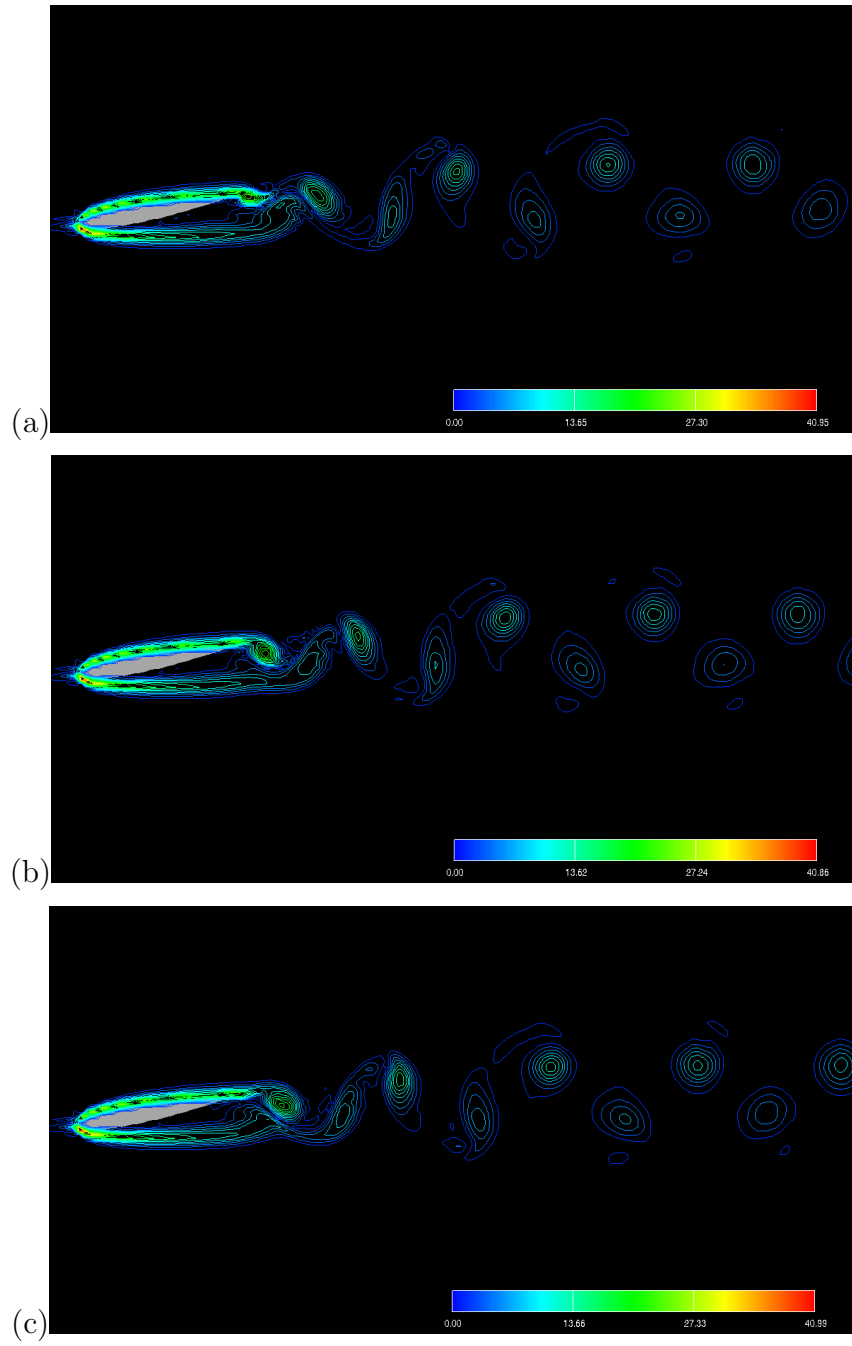
Figure D.10: Contours of absolute value of vorticity near the rigid airfoil at $-10°$ angle of incidence at:(a)minimum downforce;(b)average downforce;(c)maximum downforce
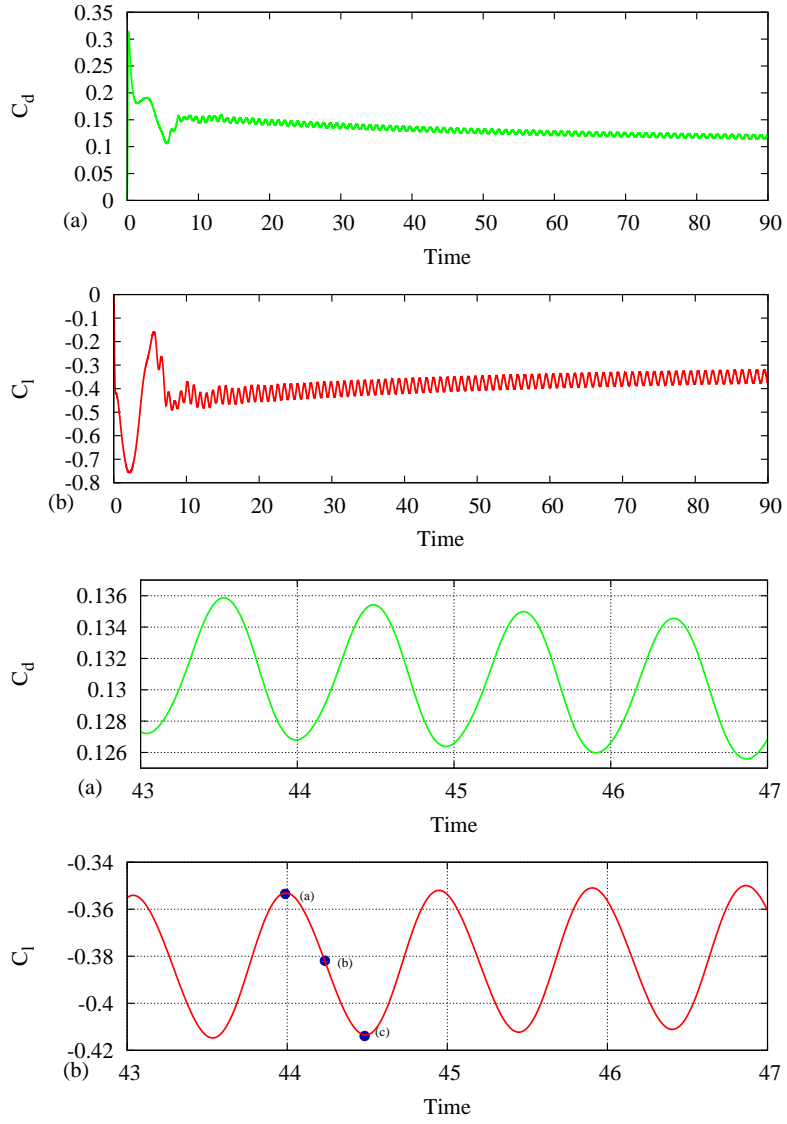
Figure D.11: Time history of lift and drag coefficient for airfoil ($E = 5.5 \times 10^6$ Pa) at $-10°$ angle of incidence:(a)minimum downforce;(b)average downforce;(c)maximum downforce
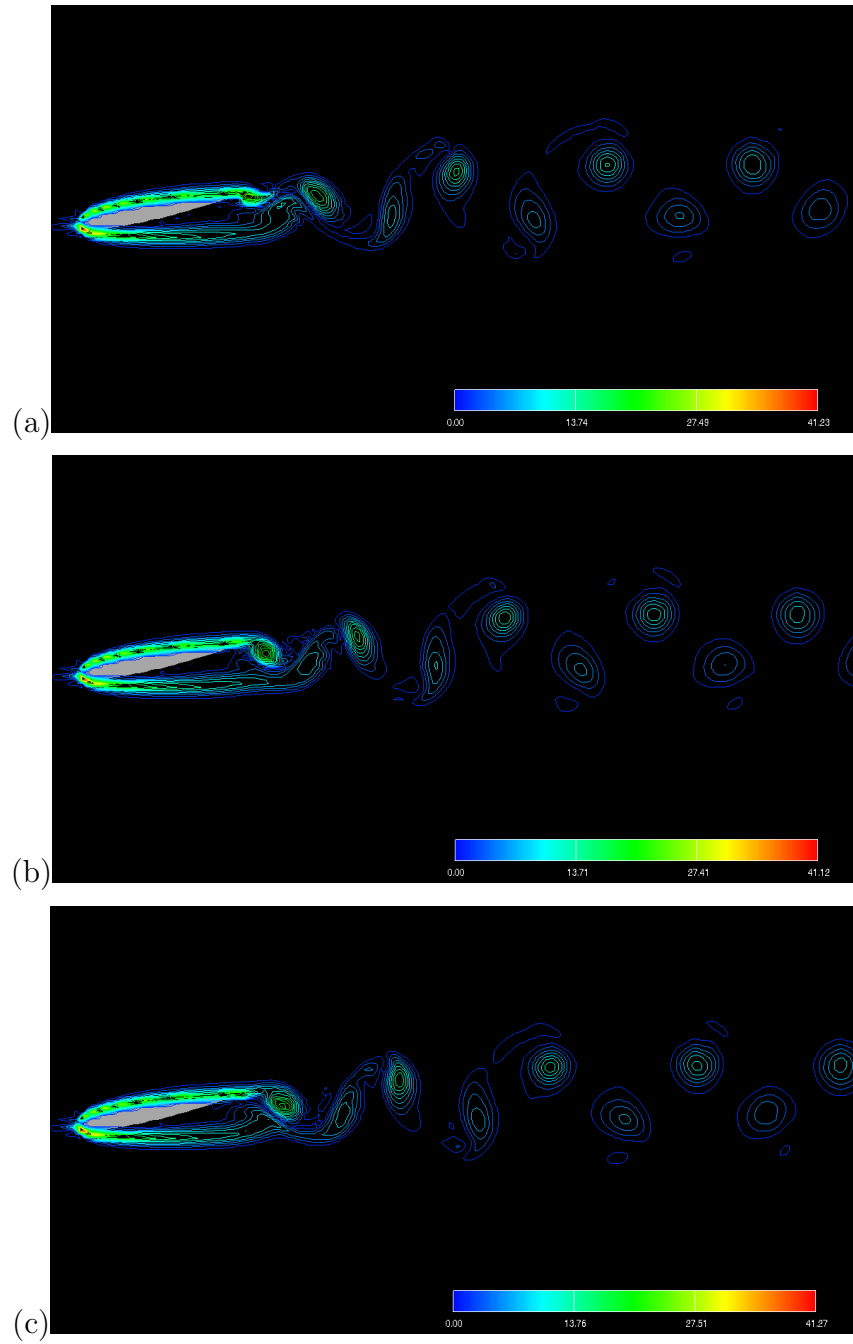
Figure D.12: Contours of absolute value of vorticity near the airfoil ($E = 5.5 \times 10^6$ Pa) at $-10°$ angle of incidence at:(a)minimum downforce;(b)average downforce;(c)maximum downforce

Figure D.13: Time history of lift and drag coefficient for airfoil ($E = 2.0 \times 10^2$ Pa) at $-10°$ angle of incidence:(a)minimum downforce;(b)average downforce;(c)maximum downforce

67

Figure D.14: Contours of absolute value of vorticity near the airfoil ($E = 2.0 \times 10^2$ Pa) at $-10°$ angle of incidence at:(a)minimum downforce;(b)average downforce;(c)maximum downforce
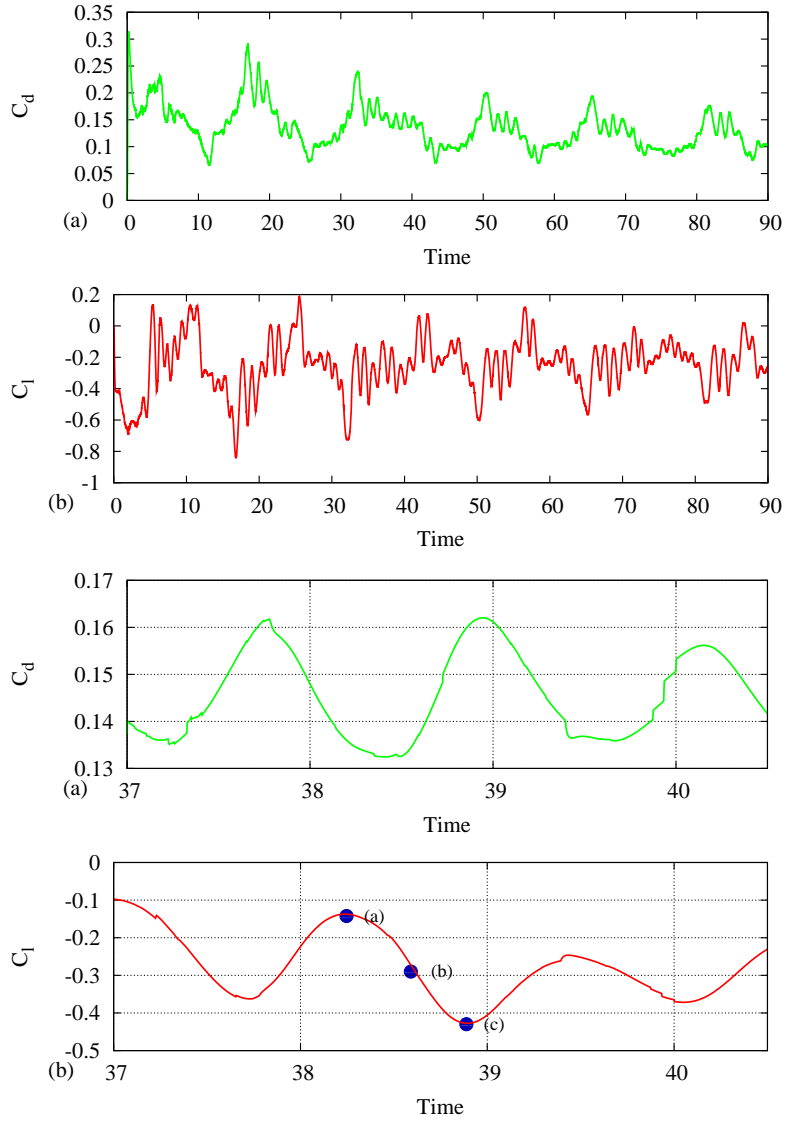
Figure D.15: Time history of lift and drag coefficient for airfoil ($E = 1.0 \times 10^2$ Pa) at $-10°$ angle of incidence:(a)minimum downforce;(b)average downforce;(c)maximum downforce
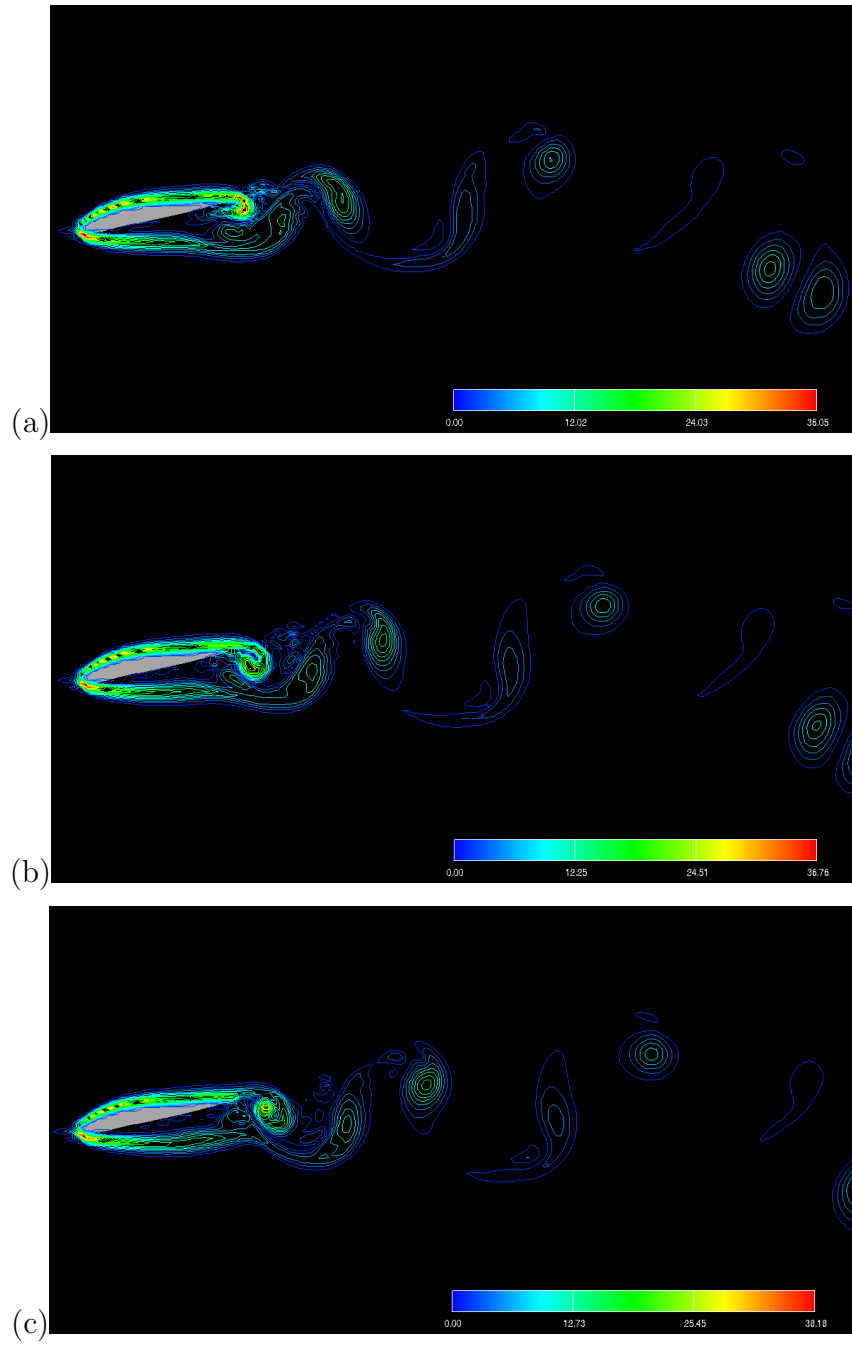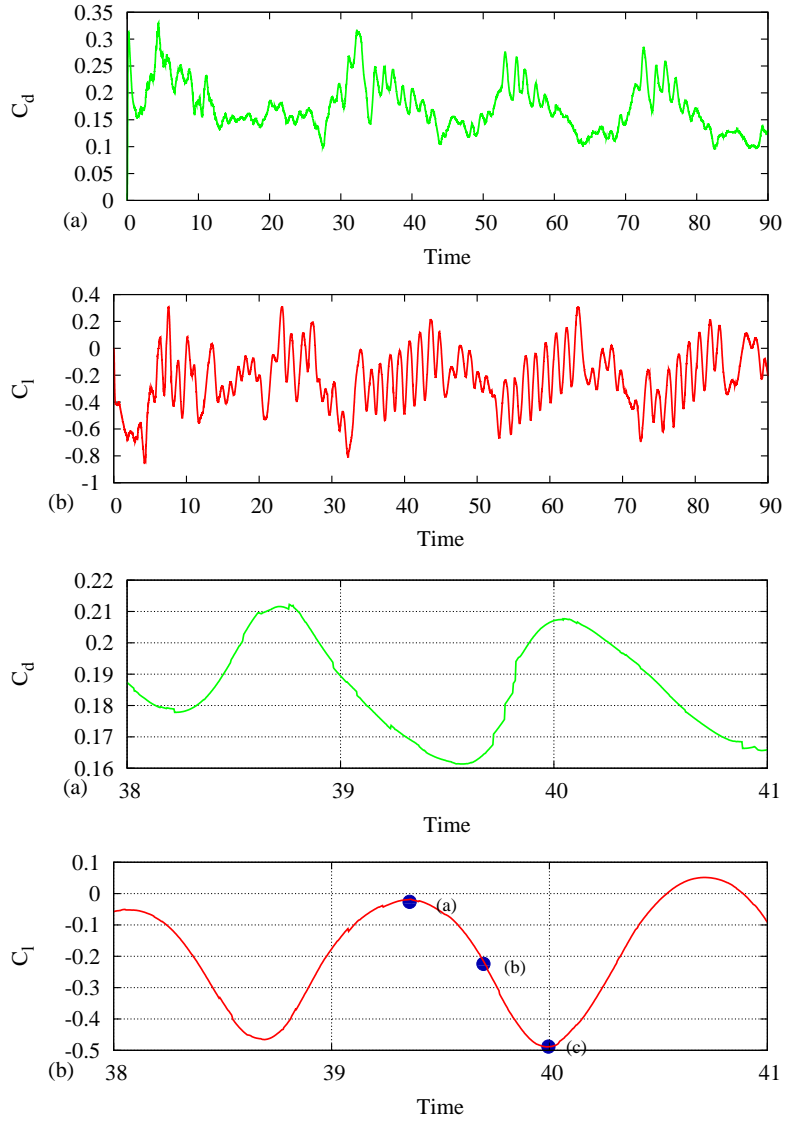
69
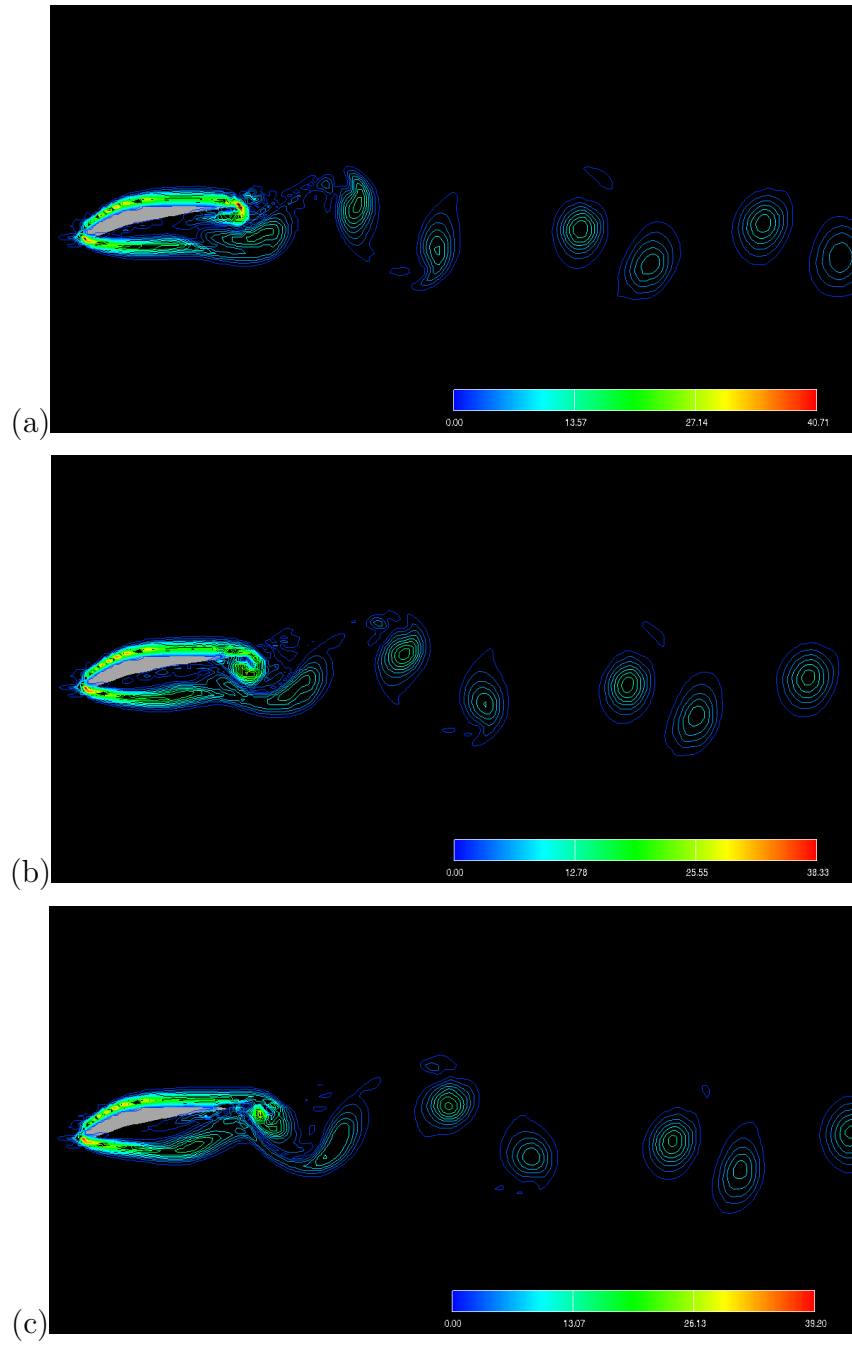
Figure D.16: Contours of absolute value of vorticity near the airfoil ($E = 1.0 \times 10^2$ Pa) at $-10°$ angle of incidence at:(a)minimum downforce;(b)average downforce;(c)maximum downforce

Bibliography

[1] Uhlmann, M., 2005. "An immersed boundary method with direct forcing for the simulation of particulate flows". *Journal of Computational Physics,* **209**(2), pp. 448–476.

[2] Gilmanov, A., and Sotiropoulos, F., 2005. "A hybrid cartesian/immersed boundary method for simulating flows with 3d, geometrically complex, moving bodies". *Journal of Computational Physics,* **207**, pp. 457–492.

[3] Peskin, C., 1972. "Flow patterns around heart valves: A numerical method". *Journal of Computational Physics,* **10**(2), pp. 252–271.

[4] L.Zhu, and Peskin, C., 2002. "Simulation of a flapping flexible filament in a flowing soap film by immersed boundary method". *J. Comp. Phys.,* **179**(2), pp. 452–468.

[5] Mendes, P., and Branco, F., 1999. "Analysis of fluid-structure interaction by an arbitrary lagrangian-eulerian finite element formulation". *International Journal for Numerical Methods in Fluids,* **30**, pp. 897–919.

[6] Zhang, Q., and Hisada, T., 2001. "Analysis of fluid-structure interaction problems with structural buckling and large domain changes by ale finite element method". *Computer Methods in Applied Mechanics and Engineering,* **190**, pp. 6341–6357.

[7] Rugonyi, S., and Bathe, K., 2001. "On finite element analysis of fluid flows fully coupled with structural interactions". *Computer Modeling in Engineering and Sciences,* **2**, pp. 195–212.

[8] Heil, M., 2004. "An efficient solver for the fully coupled solution of large-displacement fluid-structure interaction problems". *Computer Methods in Applied Mechanics and Engineering,* **193**, pp. 1–23.

[9] Ishihara, D., and Yoshimura, S., 2005. "A monolithic approach for interaction of incompressible viscous fluid and an elastic body based on fluid pressure poisson equation". *International Journal of Numerical Method Engineering,* **64**, pp. 167–203.

[10] Stein, K., Benney, R., Kalro, V., Tedzuyar, T. E., Leonard, J., and Accorsi, M., 2000. "Parachute fluid-structure interaction: 3-d computation". *Computer Methods in Applied Mechanics and Engineering,* **190**, pp. 373–386.

[11] Kalro, V., and Tedzuyar, T., 2000. "A parallel 3d computational method for fluid-structure interaction in parachute systems". *Computer Methods in Applied Mechanics and Engineering,* **190**, pp. 321–332.

[12] Gluck, M., Breuer, M., Durst, F., Halfmann, A., and Rank, E., 2001. "Computation of fluid-structure interaction on lightweight structures". *Journal of Wind Engineering and Industrial Aerodynamics,* **89**, pp. 1351–1368.

[13] Park, K., Felippa, C., and Ohayon, R., 2001. "Partitioned formulation of internal fluid-structure interaction problems by localized lagrange multipliers". *Computer Methods in Applied Mechanics and Engineering,* **190**, pp. 2989–3007.

[14] Matthies, H., and Steindorf, J., 2003. "Partitioned strong coupling algorithms for fluid-structure interaction". *Computers and Structures,* **81**, pp. 805–812.

[15] Hirt, C., Amsden, A., and Cook, J., 1974. "An arbitrary lagrangian-eulerian computing method for all flow speed". *Journal of Computational Physics,* **14**(3), pp. 227–253.

[16] Peskin, C., 2002. "The immersed boundary method". *Acta Numerica*, pp. 1–39.

[17] Kajishima, T., Takiguchi, S., Hamasaki, H., and Miyake, Y., 2001. "Turbulence structure of particle-laden flow in a vertical plane channel due to vortex shedding". *JSME International Journal Series B - Fluids and Thermal Engineering,* **44**(4), pp. 526–535.

[18] Mohd-Yusof, J., 1997. "Combined immersed-boundary/b-spline methods for simulations of flow in complex geometries". *CTR Annual Research Briefs, Center for Turbulence Research, NASA Ames/Stanford Univ*, pp. 317–327.

[19] Fadlun, E., R.Verzicco, Orlandi, P., and Mohd-Yusof, J., 2000. "Combined immersed-boundary finite-difference methods for three-dimensional complex flow simulations". *Journal of Computational Physics,* **161**(1), pp. 35–60.

[20] Kim, D., and H.Choi, 2006. "Immersed boundary method for flow around an arbitrary moving body". *Journal of Computational Physics,* **212**, pp. 662–680.

[21] Boujo, E., Tuan-Ya, T. M. Y. S., Takeuchi, S., and Kajishima, T., 2006. "Study of fluid-structure interaction problems involving deformable objects by a new finite element - immersed boundary approach". *The Third International Symposium on Aero Aqua Bio-Mechanics (ISABMEC2006)*, July 3-7, p. Paper No. 225.

[22] Boujo, E., 2006. *Finite Element - Immersed boundary approach for simulation of fluid-structure interaction problems involving deformable objects.* Graduate thesis of Royal Institute of Technology (KTH), Stockholm, Sweden.

[23] Kim, J., and Moin, P., 1985. "Application of a fractional-step method to incompressible navier-stokes equations". *Journal of Computational Physics,* **59**, pp. 308–323.

[24] Yuki, Y., Takeuchi, S., and Kajishima, T., 2007. "Efficient immersed boundary method for strong interaction problem of arbitrary shape object with the self-induced flow". *Journal of Fluid Science and Technology,* **2**(1), pp. 1–11.

[25] M.Drela, 2001. *XFOIL 6.94 User Guide.*

[26] Kinsler, L., Frey, A., Coppens, A., and Sanders, J., 1982. *Fundamental of Acoustic, 3rd Edition.* Wiley.

[27] Lin, M. C., and Manocha, D., eds., 1996. Triangle: Engineering a 2D Quality Mesh Generator and Delaunay Triangulator, in Applied Computational Geometry: Towards Geometric Engineering, Vol. 1148 of *Lecture Notes in Computer Science*, Springer-Verlag.